A Single-Cell Bioprinting Approach with Subcellular Resolution to Reconstruct Native Cellular Microenvironments and Interrogate Spatial Biology

Haylie R. Helms[1,2,3], Kody A. Oyama[1], Alexander E. Davies[1,3,4,5], Ellen M. Langer[1,3,4,6], and Luiz E. Bertassoni[1,2,3,4,7,8,9]*

[1]Knight Cancer Precision Biofabrication Hub, Knight Cancer Institute, Oregon Health and Science University, Portland, OR 97201, USA
[2]Department of Biomedical Engineering, School of Medicine, Oregon Health and Science University, Portland, OR 97201, USA
[3]Cancer Early Detection Advanced Research Center (CEDAR), Knight Cancer Institute, Oregon Health and Science University, Portland, OR 97201, USA
[4]Division of Oncological Sciences, Knight Cancer Institute, Oregon Health and Science University, Portland, OR 97201, USA
[5]Department of Pediatrics, School of Medicine, Oregon Health and Science University, Portland, OR, 97201, USA
[6]Molecular and Medical Genetics, School of Medicine, Oregon Health and Science University, Portland, OR, 97201, USA
[7]Division of Biomaterials and Biomechanics, Department of Oral Rehabilitation and Biosciences, School of Dentistry, Oregon Health and Science University, Portland, OR 97201, USA
[8]Center for Regenerative Medicine, School of Medicine, Oregon Health and Science University, Portland, OR 97201, USA
[9]Lead Contact
*Correspondence: bertasso@ohsu.edu

SUMMARY

Tissue development, function, and disease are largely driven by the spatial organization of individual cells and their interactions within a complex and heterogeneous cellular microenvironment. Engineered tissue models provide a controllable platform to dissect these spatially driven processes. However, strategies to fabricate tissues that replicate near-exact spatial organization and cellular composition of native microenvironments, necessary to faithfully recapitulate in vivo spatial relationships, have remained elusive to date. Here we present a precision bioprinting approach capable of generating high-fidelity replicas of patient biopsies that preserve complex cellular organization and heterogeneity with subcellular resolution. We demonstrate spatial placement of individual cells with down to ~3 μm spatial precision and up to eight cell types per bioprint. Using this approach, we demonstrate for the first time that altering the microscale spatial organization of tumor microenvironments of similar cellular composition can significantly alter transcriptomic programs of cell response. The ability to engineer and manipulate native cellular microenvironments with single-cell resolution marks a significant advancement toward understanding the critical influence of spatial biology on complex biological systems, such as the tumor microenvironment and organogenesis.

GRAPHICAL ABSTRACT

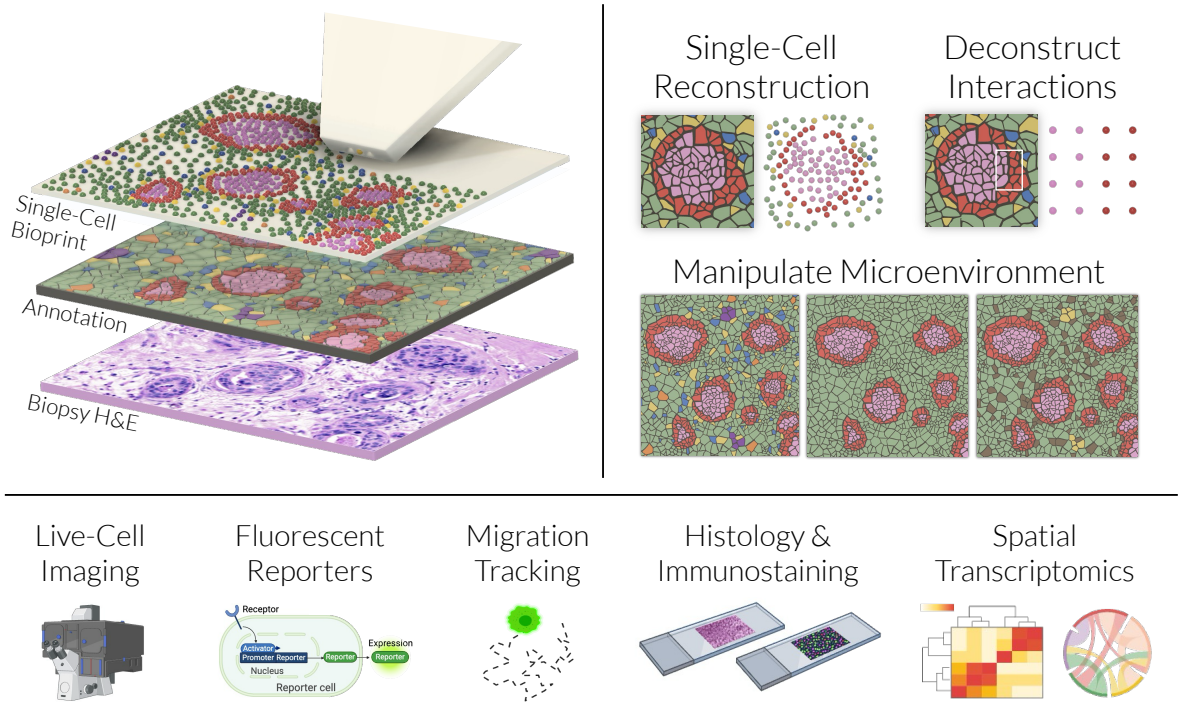

INTRODUCTION

In vitro models serve a vital role in interrogating fundamental cell biology, modeling disease, and informing the development of new therapies. Although tissue engineering has enabled fabrication of increasingly complex tissues to recapitulate key aspects of native architecture and function[1,2], including the ability to manipulate single cells[3-12], technologies capable of reproducing the spatial organization of native cellular microenvironments with single-cell spatial resolution have yet to be demonstrated. Current in vitro cell culture models, such as organoids and plated co-cultures, depend on stochastic cellular self-organization that can artifactually introduce interactions between cell types that would not normally occur in vivo.[13] Similarly, three-dimensional (3D) culture models, like cell-laden hydrogel bioprinting or lithography-based micropatterning, lack sufficient resolution needed to ensure that precise cell-cell spatial relationships are reproduced at the single cell level.[2] These limitations risk the loss of critical functional interactions during tissue formation, limiting translatability by producing biological outputs that diverge from ground truth in vivo behavior.[13]

The significance of cellular spatial organization on the fate and function of complex biological systems has been repeatedly demonstrated through recent advances in spatial

-omic technologies.[14-16] Clinically, studies have shown that cell type, density, and spatial arrangement are key determinants of disease progression, treatment response, and development.[17-21] In native tissues, even small differences in cell positioning can alter biological programs, signaling dynamics, and phenotypic outcomes.[22-25] Therefore, experimental platforms capable of precisely replicating and manipulating single-cell spatial organization of native tissues in vitro have immense potential for a range of applications, such as dissecting the spatial logic of cell-cell communication, mapping spatial rules of cell state transitions, and generating ground-truth data to train predictive in silico models.

Here, we develop and optimize an approach using a microfluidic single-cell bioprinting platform for the fabrication of heterogeneous tissue models containing up to 8 cell types and 3.14 μm spatial precision to mimic the precise organization of the multicellular microenvironment in a native tissue. We demonstrate, for the first time, the feasibility of characterizing a region of interest in a complex patient tissue biopsy, identifying the coordinates of each cell, and reproducibly fabricating accurate replicas of tissue structures with unmatched spatial accuracy (**Figure 1A**). Additionally, we utilize single cell spatial transcriptomic analyses with live-cell imaging and immunofluorescence of engineered reporters to demonstrate how the cell-cell interactions established by the single-cell spatial patterning of tissue constructs can significantly influence cell crosstalk and transcriptional identities. We argue that this platform opens a new chapter in tissue biofabrication and spatial biology, where heterogeneous tissue models, such as the tumor microenvironment in solid malignancies, can be built with reproducibility and control. These tissues allow for the systematic dissection of cell-cell interactions in complex tissue contextures, down to the individual cell, driving development, disease, and therapeutic response.

DESIGN

Motivated by the insights gained from spatial biology studies, we set out to develop a biofabrication platform capable of faithfully recreating regions of interest from patient tissues with experimental flexibility and reproducibility. Existing approaches, such as explant cultures and retrospective analysis of banked tissues, provide invaluable

biological insights but are constrained by tissue availability and offer limited experimental control to perturb local cell–cell interactions and tissue architecture in a systematic manner to establish cause–effect relationships.

To successfully match the cellular and spatial complexity of native tissue structures in vitro we prioritized the following design criteria: i) Reproducibly pattern exactly one cell per spot, no multiples or blanks. ii) Bioprint cells in any geometric configuration, unconstrained by predefined XY grid pattern. iii) Controllably deposit cells with intercellular spacing below the diameter of a single cell (~18 μm) to achieve the resolution necessary to recreate physiologic tissue organization. iv) Multiplex to deposit at least four cell types without stopping the bioprinting process, to replicate complex tissue heterogeneity. Because our goal was to establish a platform technology, we also prioritized fabrication approaches that were v) compatible with a wide variety of cell types and biomaterials and vi) amenable to a variety of downstream experimental methods such as live-cell manipulation (i.e., live-seq[26], single-cell dosing[27], patch clamp), imaging, and sample extraction.

To meet the above criteria, we assessed technologies that could manipulate single cells with high precision and control, including a laser assisted-forward transfer bioprinter (NGB-R, Poietis), inkjet single cell dispenser (D100, HP), robotic single cell picking system (CellCelector, Sartorius), and open volume microfluidic cell dispenser (Biopixlar, Fluicell), all available in our lab and described in the literature (**Table S1**). While the available systems could not meet all our design criteria, the microfluidic cell dispenser showed the most promise. We therefore set out to define a set of engineering parameters that would allow controlled and reproducible transport of heterogeneous cell singlets for patterning of virtually unlimited spatial configurations on substrates ranging from hydrogels to tissue culture plastic.

The flow of the microfluidic dispenser is controlled by four independent parameters (delivery pressure, non-delivery pressure, internal vacuum, and external vacuum), accounting for over two billion possible combinations, that remained to be defined for heterogeneous single-cell bioprinting (**Figures 1B and S1**). We began by identifying flow parameters that would support controlled single-cell dispensing out of the printhead, before interrogating cell attachment strategies. Complete details of the microfluidic

dispenser, experimental design, and rationale are provided in **Supplementary Information File 2**. In brief, cells are suspended in complete cell culture medium and loaded into the microfluidic device (printhead). Each device contains four independent reservoirs (**Figure S1B**) which are maintained under continuous laminar flow through the device. The four flows converge at the crossover zone where they interface with the aspiration (internal vacuum) channels (**Figure S1C**). When the pressures are properly tuned, only the flow from the desired reservoir will exit the device, while the remaining flows are diverted into the aspiration channels (**Figure S1D**). Adequate balance of positive delivery pressure and external aspiration creates a controlled liquid-liquid boundary (recirculation zone) that allows the tip of the printhead to be continuously submerged in culture medium as single cells are dispensed and readily adhere to the substrate (**Figures 1B and S1D).**

Since cells add significant variability to flow (i.e., cell size and shape, tendency to aggregate, sedimentation leading to changing concentration of the dispensed solution), we first sought to identify conditions which produce a stable recirculation zone for controlled delivery using only the liquid medium (**Figures 1C-D and S2; Video 1**). Of these successful combinations, we then added cells to the medium and asked which of these conditions allow cells to be consistently dispensed (**Figures 1E and S3A-B**). Next, we asked which conditions ensure only cells from the correct wells were controllably dispensed (**Figures 1F and S3C-E**).

The conditions that passed these three tests were then investigated for their ability to controllably and reproducibly pattern single cells onto a substrate. Cells attach to their culture substrate through two primary mechanisms: integrin-mediated binding to an extracellular matrix protein and/or electrostatic interaction with a positively charged surface. Cells continue to freely flow through the recirculation zone unless contact is made with a suitable substrate, or there is sufficient electrostatic pull to bring it to the substrate. We sought to determine the cell dispensing factors that enabled attachment immediately after dispensing to prevent lateral drift that would reduce printing accuracy. We added a heating unit to maintain temperatures at 37 °C to support cell health and enhance binding kinetics. We also adjusted the angle of the printhead to a maximum angulation to facilitate maximal cell-matrix contact. To achieve our desired resolution, we

also developed custom software in which the bioprint design template could be projected onto the live microscope feed and defined printhead movement relative to the design.[28] After integrating these modifications, we then bioprinted primary human umbilical vein endothelial cells (HUVEC) onto a collagen substrate and assessed printability based on the binding success, ability to deposit a single cell vs doublet(s), and bioprinting speed (**Figure S4**). We identified 80 mbar delivery pressure, 0 mbar non-delivery, -25 mbar internal vacuum, and -40 mbar external vacuum, in combination with a 70º printhead and chamber heating unit, to be an ideal combination of parameters thus establishing a single-cell bioprinting platform that can pattern individual cells with precision and control.

RESULTS

Single-cell bioprinting enables micron-scale spatial control, multiplexing, and broad compatibility

Our driving motivation for developing the single-cell bioprinting platform was to create heterogeneous tissue constructs that 1) precisely replicate native cellular microenvironments with near-exact spatial accuracy, 2) enable controlled experimentation of biological relationships that are dependent on cell spatial organization, and 3) can be built on demand. We approached this by first refining our ability to controllably manipulate the spatial organization of cells in space with precision and heterogeneity, then incrementally build toward tissue level complexity (**Figure 1G**). Using the bioprinting parameters established above, we bioprinted individual prostate cancer cells to write the name of our university (“OHSU”) (**Figure 1H**) to illustrate controlled, single-cell deposition without any doublets or missing spots (design criteria i) and freeform geometry (design criteria ii). To demonstrate our ability to controllably space cells (design criteria iii), we then bioprinted the Fibonacci sequence, also known as the golden ratio, using a mammary epithelial cell line (MCF10A) (**Figure 1I**). At the smallest point, cells were positioned with an edge-to-edge (intercellular) spacing of 1.3 μm. This represents an order-of-magnitude reduction in intercellular spacing compared to existing inkjet and laser-assisted bioprinting approaches, which report high positional accuracy (i.e., within

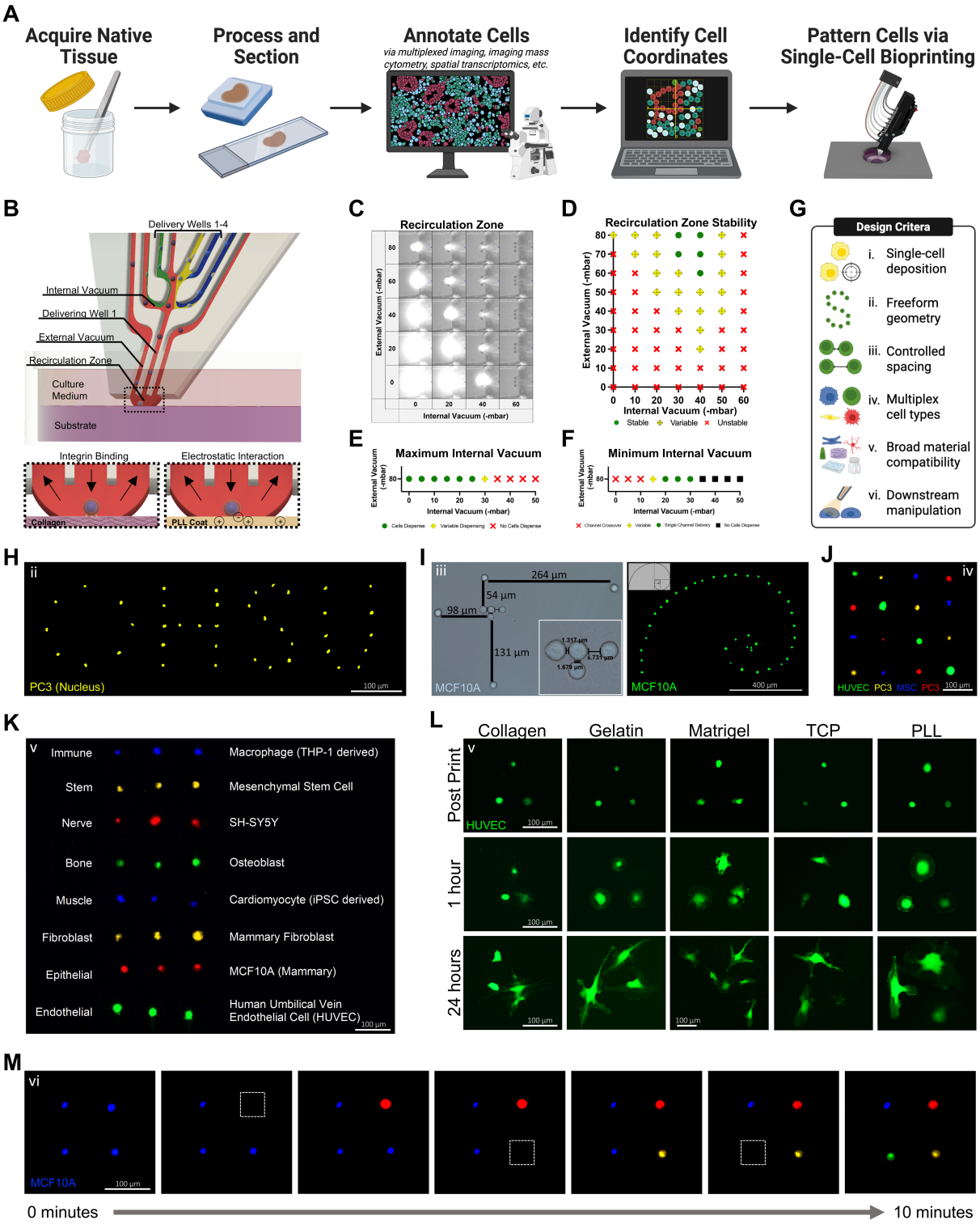

Figure 1. Single-cell bioprinting approach development and demonstration

(A) Workflow to reconstruct native cellular microenvironments with single-cell resolution. Annotated map adapted with permission.[29] 2020, Springer Nature.

(B) Microfluidic print head schematic showing internal fluidic paths, vacuum interfaces, cell delivery, and cell attachment mechanisms.

(*legend continued on next page*)

(C) Visualization of the recirculation zone by flowing fluorescein through transparent medium at 80 mbar delivery pressure.
(D) Recirculation zone stability across different print heads at 80 mbar delivery pressure. $n = 3$.
(E) Maximum internal vacuum which allows cell dispensing at 80 mbar delivery pressure. $n = 9$.
(F) Minimum internal vacuum that prevents unwanted dispensing from other wells at 80 mbar delivery pressure. $n = 9$.
(G) Fabrication design criteria (i-vi) to recreate native cellular microenvironments with single-cell resolution.
(H-M) Design criteria i, single-cell deposition. Each spot is an individual human cell, no doublets or blank spots.
(H) Design criteria ii, bioprinting cells in any geometry unconstrained by predefined XY grid patterns. Single prostate cancer cells (PC3) with fluorescent nuclear stain imaged immediately after printing, before cells have spread. Scale bar, 100 µm.
(I) Design criteria iii, Fibonacci sequence illustrating controlled spacing. Mammary epithelial cells (MCF10A) with fluorescent cell tracker imaged immediately post bioprint. Scale bar, 400 µm.
(J) Design criteria iv, multiplex cell types. Heterotypic array containing four cell populations bioprinted in a single run and imaged immediately post bioprint. Scale bar, 100 µm.
(K-L) Design criteria v, broad cell and substrate compatibility. (K) Eight of the common cell types found in the body patterned in one bioprint, each fluorescently tagged prior to bioprinting to enable identification. Image taken immediately after bioprinting. Scale bar, 100 µm. (L) GFP+ human umbilical vein endothelial cells (HUVEC) bioprinted onto collagen, gelatin, Matrigel, tissue culture plastic (TCP), and poly-L-lysine (PLL) coated tissue culture plastic. Cells bind to collagen, gelatin, and Matrigel via integrin binding. Cells attach to TCP and PLL through electrostatic interaction. Scale bars, 100 µm.
(M) Design criteria vi, downstream amendability. Sequence demonstrating controlled single-cell manipulation using the recirculation zone. A single mammary epithelial cell (MCF10A) was selectively detached using TrypLE, followed by deposition of a new MCF10A at the same coordinate. Scale bar, 100 µm.

10 µm of intended target[6]) but rely on substantially larger spacing (i.e., 50 µm[5]) to achieve reproducible placement. Finally, heterotypic tissues require multiplexed bioprinting that enables on-demand switching between cell types within a single print run, rather than sequential single-material runs that require reloading or restarting the print for each cell type (design criteria iv). Unlike other high precision cell patterning strategies which can only support one cell type at a time, this platform can simultaneously bioprint 4 different cell types without having to swap the loaded material. Endothelial cells (HUVEC), mesenchymal stem cells (MSCs), and prostate cancer cells (PC3, fluorescently tagged two different colors) were loaded into the printhead and bioprinted into an array of alternating cell populations to demonstrate multiplexing capability (**Figure 1J**). This also served as confirmation that the bioprinting parameter selection was robust to deliver the correct cell type without unwanted crossover of cell populations mid-print, which is key to ensuring precision during reconstruction and mimicking of tissue microenvironments with single cell positional accuracy.

Since our goal was to be able to recreate native tissue microenvironments, it was critical that the platform be compatible with many cell types and materials (design criteria v). As proof of concept, we patterned eight of the most common cell lineages (immune, stem, nerve, bone, muscle, fibroblast, epithelial, and endothelial), fluorescently tagged

prior to bioprinting to facilitate cell type identification, onto a collagen substrate in a single bioprint using two printheads (**Figure 1K**). The established bioprinting conditions reliably supported all cell types tested, despite differences in physical properties such as cell size and aggregation behavior which add variability to the fluid regime, underscoring the robustness of the approach. We then investigated compatibility with a range of substrates. HUVECs were bioprinted onto collagen, gelatin, Matrigel, tissue culture plastic, and poly-L-lysine (PLL) coated tissue culture plastic with 100 μm spacing between cells (**Figure 1L**). Cell spreading and migration were observed within one hour of bioprinting, thus indicating adequate cell health. We also observed occasional division within that hour, which indicated the bioprinting process did not induce sufficient stress that would cause the cell to exit the cell cycle. The bioprints were imaged again at 24 hours showing the expected cell morphology, migration, and the observed population doubling of the Matrigel group.

Finally, to demonstrate facilitated downstream analysis such as single cell sampling or manipulation (design criteria vi), the fabrication approach was designed to pattern cells in defined spatial positions without requiring cell encapsulation. Using the confined recirculation zone produced by the printhead, we demonstrated the ability to manipulate a single cell after sample fabrication by flowing a cell detachment agent (TrypLE) over one cell, without disrupting the neighboring cells[27], until it detached (**Figure 1M**). The cell was then aspirated by the external vacuum, and a new cell (note different color) was deposited into its place. Additionally, we demonstrate that cells can also be encapsulated in a hydrogel layer after bioprinting, and three dimensional constructs can be fabricated one layer at a time (**Figure S5**).

Controlled perturbation of cellular arrangement and composition reveals spatially dependent migration behaviors

Having established a platform capable of reproducibly patterning single cells with high spatial precision, we next sought to demonstrate how this approach enables the controlled and systematic manipulation of microenvironment features that determine spatial biology effects, such as cellular arrangement and composition, which have been shown to correlate with clinical outcomes in retrospective studies.[17-25]

As an initial proof of concept, motivated by published clinical observations that dispersed versus clustered tumor architectures associate with divergent patient outcomes[30,31], triple negative breast cancer (MDA-MB-231) and endothelial cells (HUVEC) were patterned into identical arrays with fixed 100 μm intercellular spacing, varying only the spatial arrangement of the two cell types (**Figure 2A**). Live-cell imaging revealed highly dynamic endothelial cell behavior, characterized by frequent interactions with cancer cells and protrusions consistent with environment sensing (**Figure 2B; Videos 2-4**). Merged migration data across replicates revealed distinct and reproducible spatially dependent patterns. While total distance traveled did not differ significantly across arrangements within a given cell type (**Figure 2C**), spatial organization influenced migration behavior (**Figures 2D-H and S6A-C**). For example, in segregated configurations, endothelial cells exhibited persistent, directed migration toward the cancer compartment, whereas in mixed configurations, endothelial cells migration was largely nondirectional, reflected by minimal net center-of-mass displacement.

We then examined how altering microenvironment cellular composition influences cancer cell migration. Triple negative breast cancer cells (MDA-MB-231) were patterned in the same array design either alone or in mixed configuration with myoepithelial cells, mammary fibroblasts, or macrophages and live-cell imaged (**Figures 2I–M and S6D-G; Videos 5-8**). Changes in microenvironment cellular composition resulted in distinct cancer migration behavior, reflected by differences in distance traveled, mean squared displacement, and mean distance to nearest non-cancer neighbor. Taken together, these results demonstrate precision-engineered microenvironments defined at the level of individual cells provide a controllable and reproducible framework for systematically interrogating cause–effect relationships in cell behavior.

Reconstruction of native cellular microenvironments at subcellular resolution

Our initial studies demonstrated independent control over fabrication capabilities required to reconstruct native cellular microenvironments, including single-cell placement, spacing, and heterogeneity; therefore we next sought to combine these capabilities to recreate a patient biopsy matching the spatial and cellular complexity at tissue scale. A region of interest from a previously annotated human breast cancer biopsy[29] was

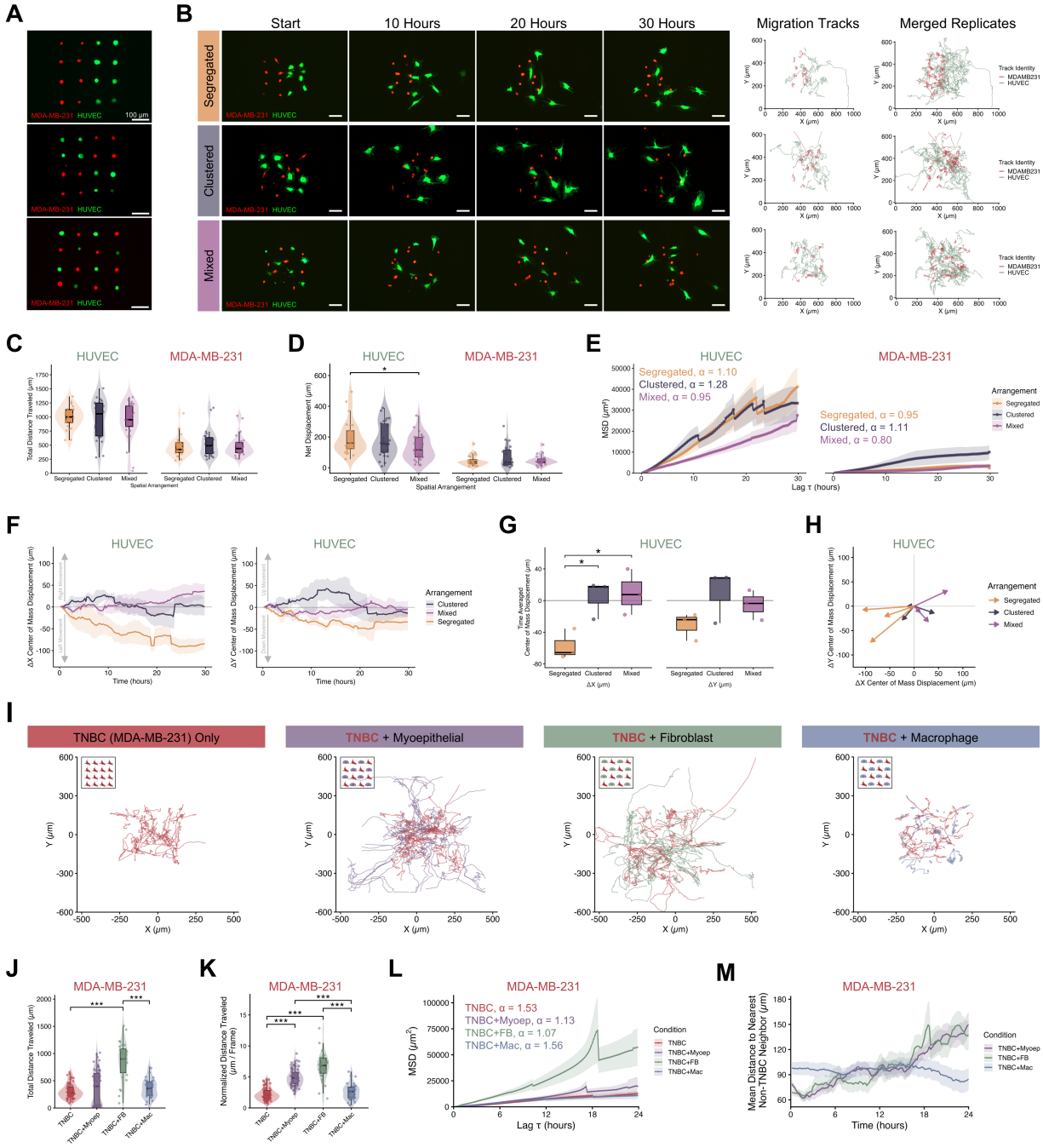

Figure 2. Cell–cell interaction arrays dissect spatial and compositional effects on single-cell migration

(A) Controlled patterning of single cells at 100 µm spacing in segregated, clustered, or mixed configurations. Triple negative breast cancer (MDA-MB-231, cell-tracker labeled) and endothelial cells (GFP+ HUVEC) imaged immediately after each bioprint. Scale bars, 100 µm.

(B-H) Effect of spatial arrangement on single-cell migration behavior in GFP+ HUVEC and MDA-MB-231 interaction arrays. n = 3 bioprinted arrays per spatial configuration.

(B) Time-lapse fluorescence images and single-cell migration trajectories. Scale bars, 100 µm.

(C) Total distance traveled (µm) of each cell.

(*legend continued on next page*)

(D) Net displacement of each cell. One-way ANOVA with Tukey's multiple-comparisons test, * $p < 0.05$
(E) Time-averaged mean squared displacement (TASD) for each spatial arrangement, plotted as mean ± SEM across cells. The anomalous diffusion exponent (α) describes the mode of migration (α < 1, sub-diffusive; α = 1, random; α > 1, persistent).
(F) HUVEC center-of-mass displacement over time along X and Y axes, plotted as mean ± SEM across bioprinted arrays.
(G) Time-averaged HUVEC center-of-mass displacement across replicates. One-way ANOVA with Tukey's multiple-comparisons test, * $p < 0.05$
(H) Center-of-mass (COM) displacement vectors for HUVEC, shown for each bioprinted array across spatial arrangements. Arrows indicate the direction and magnitude of net collective displacement in the X–Y plane.
(I-M) Effect of cellular composition on triple negative breast cancer (MDA-MB-231) migration in mixed configuration arrays containing either myoepithelial cells, fibroblasts, macrophages, or MDA-MB-231 (control) at 100 μm spacing. n = 4 arrays per group, except TNBC+Fibroblast (n = 3).
(I) Merged migration tracks of mixed configuration arrays containing MDA-MB-231 and either myoepithelial, fibroblast, macrophage, or MDA-MB-231 (control).
(J) Total distance traveled of each MDA-MB-231 cell. Welch ANOVA with Benjamini–Hochberg corrected Welch pairwise t-tests; * $p < 0.05$, ** $p < 0.01$, *** $p < 0.001$.
(K) Normalized distance traveled of each MDA-MB-231 cell (μm / frame), which corrects for distances truncated by cell division or migration out of the field of view. Welch ANOVA with Benjamini–Hochberg corrected Welch pairwise t-tests; * $p < 0.05$, ** $p < 0.01$, *** $p < 0.001$.
(L) MDA-MB-231 time-averaged mean squared displacement (TASD) for each spatial arrangement, plotted as mean ± SEM across cells. The anomalous diffusion exponent (α) describes the mode of migration (α < 1, sub-diffusive; α = 1, random; α > 1, persistent).
(M) Mean distance from each MDA-MB-231 cell to its nearest non-MDA-MB-231 neighbor over time, plotted as mean ± SEM across cells.

selected, containing malignant mammary epithelial cells with surrounding stromal compartment (**Figure 3A**). As proof of concept for the ability to reconstruct native tissue architecture, cell coordinates were extracted to generate a high-fidelity bioprint map for placement of five distinct cell types: mammary epithelial cells (MCF10A), triple negative breast cancer (MDA-MB-231), mammary fibroblasts, mesenchymal stem/stromal cells, and macrophages. Across four bioprints, the mean absolute distance between intended target position (bioprint map) and bioprinted cell position was 3.14 ± 2.93 μm, with 99.62% of the measured points within one cell diameter (≤18 μm) of the intended location (**Figures 3B-E and S7A**). These measurements demonstrate reconstruction of native cellular microenvironments with subcellular accuracy, preserving both cellular identity and spatial organization.

Live-cell imaging of the reconstructed tumor microenvironment confirmed preserved cell viability, with cells rapidly adopting expected morphologies, migrating, and proliferating over time (**Video 9; Figure S7B**). MCF10A cells displayed especially characteristic morphology, closely mirroring the native biopsy, as they quickly formed contacts with neighboring epithelial cells (**Figure 3E).** Over time, cells began migrating outward into unoccupied regions of the substrate, spreading in the absence of physical constraints that normally limit tissue expansion in vivo. We therefore reasoned increased

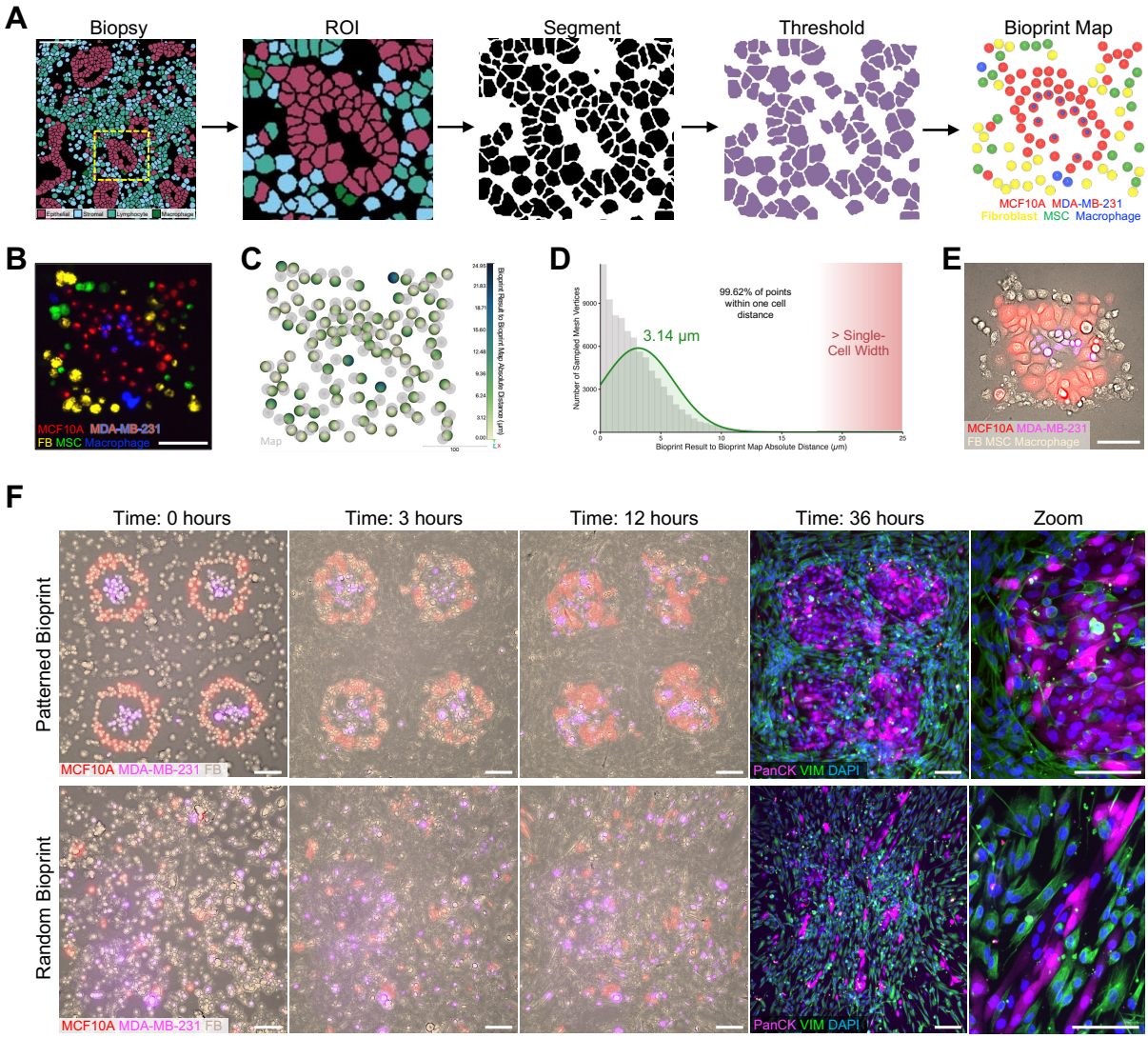

Figure 3. Single-cell reconstruction of native cellular microenvironment with subcellular resolution and the impact of spatial patterning on cellular self-assembly

(A) Workflow for generating a single-cell bioprint map from an annotated breast cancer biopsy. Biopsy adapted with permission.[29] 2020, Springer Nature.

(B) Resulting single-cell bioprint. Each cell type was fluorescently tagged prior to bioprinting; MCF10A (red), MDA-MB-231 (red + blue), fibroblasts (yellow), mesenchymal stem/stromal cells (green), and macrophages (blue). Scale bar, 100 µm.

(C) Bioprint fidelity assessment comparing bioprint result to bioprint map (gray) spatial deviation (µm). Absolute distances. Scale bar, 100 µm.

(D) Spatial accuracy across samples. Distribution of absolute distances between the bioprint result and reference bioprint map, computed from mesh vertices to the reference mesh surface. Single-cell diameter cutoff set at 18 µm. $n = 4$.

(E) Single-cell reconstruction of the same bioprint map, using cells without cell tracker dyes. EF1α + MCF10A (red) and H2B + MDA-MB-231 (pink). Scale bar, 100 µm.

(F) Comparison of patterned bioprint and random bioprint of the same cell ratios, mimicking standard co-culture, containing MCF10A, MDA-MB-231, and mammary fibroblasts. Live-cell imaging timepoints (left) and endpoint immunofluorescence staining for pan-cytokeratin (PanCK), vimentin (VIM), and DAPI (right). Scale bars, 100 µm.

cellular density would promote architectural stability. To test this, we bioprinted an idealized tissue configuration consisting of an epithelial ring (MCF10A) surrounding triple negative breast cancer cells (MDA-MB-231), encased within a dense stromal fibroblast compartment (**Figure S7C-D**). Immunostaining at 72 hours confirmed the persistence of epithelial ring-like structures surrounded by stromal cells (**Figure S7D**), demonstrating that densely patterned architectures can support prolonged maintenance of prescribed spatial organization.

Spatial patterning drives divergent architecture, transcriptional programs, and signaling networks

Many in vitro models rely on the capacity of cells to self-organize into tissue-like structures, raising the question of whether explicit single-cell spatial control is necessary. To explore this, we performed a head-to-head comparison of patterned bioprints versus stochastically arranged cells (same ratio of cells mixed in one delivery well, bioprinted at random locations), thus mimicking standard co-culture models (**Figure 3F; Videos 10-11**). Despite the same starting cell ratios, the two conditions diverged markedly in cellular morphology, organization, and local density. Patterned bioprints preserved epithelial architecture, with fibroblasts organizing circumferentially around epithelial nest-like structures. In contrast, random co-cultures failed to self-assemble into hallmark architectural features of native tissues. Additionally, fibroblast elongation appeared to bias the migration of neighboring epithelial cells, resulting in disruption of the characteristic epithelial cobblestone morphology.

To further investigate the effect of spatial patterning on cell state and transcriptional signature, we then performed single cell spatial transcriptomic analysis (Visium HD) on patterned tumor microenvironments vs randomly bioprinted co-cultures (**Figures 4 and S8**). The dataset was manually annotated using endpoint fluorescence images, in which each cell type was transduced to express a unique fluorescent protein (**Figures 4A and S8A–B**), as conventional annotation approaches deviated significantly from these fluorescence-defined ground truth labels (**Figure S8C**). Although both conditions were initiated with the same cell type ratios, endpoint population analysis revealed that random co-cultures diverged in cellular composition, with expansion of the cancer (MCF7)

population and reduced representation of mammary epithelial (MCF10A) cells (**Figure 4B**). This highlights a limitation of conventional co-culture models, which lack reproducible control over resulting cell populations, and suggests that random organization preferentially supports cancer cell expansion compared to patterned constructs in which healthy epithelial cells surrounded the cancer cells. Canonical cell marker genes identified from internal single-population controls mapped as expected across the bioprinted tissues, further supporting the manual cell type annotations (**Figures 4C and S8D-E**).

We then asked how spatial organization reshapes transcriptional programs at the tissue scale. To address this, we performed Gene Ontology Biological Process (GO-BP) enrichment on genes differentially expressed between patterned and random bioprints across all barcodes. Strikingly, the top enriched processes diverged substantially between conditions after only 24 hours of culture, with no overlap among the top 12 terms (**Figure 4D**). Patterned constructs were enriched for programs associated with tissue organization and homeostasis, including extracellular matrix organization, epithelial morphogenesis, and cell–substrate adhesion. In contrast, random bioprints were dominated by proliferation- and RNA-processing-associated signatures, including DNA replication, RNA splicing, and mitotic cell-cycle progression.

We next examined how the microenvironment experienced by individual cell types shapes pathway activity associated with core cancer hallmarks.[32] Single spot gene set enrichment analysis (ssGSEA) of cancer hallmark pathways revealed environment dependent shifts across all three cell populations (**Figure 4E and S8F-I**). Notably, samples bioprinted with random cellular spatial organization exhibited greater variability across replicates. In patterned bioprints, mammary epithelial cells (MCF10A) were positioned to surround the cancer compartment and exhibited higher mean apical junction pathway activity compared to random bioprints (**Figure S8F-G**). Similarly, breast cancer cells (MCF7) surrounded by mammary epithelial cells in patterned bioprints expressed higher mean P53 pathway activity relative to random (**Figure S8F,H**). Random organization was associated with upregulation of proliferative hallmark pathways across cell types, including E2F targets, G2M checkpoint, and MYC targets, with the strongest and most consistent increases observed in fibroblasts (**Figure SF,I**). Comparison to internal single-population controls confirmed that these pathway shifts reflect

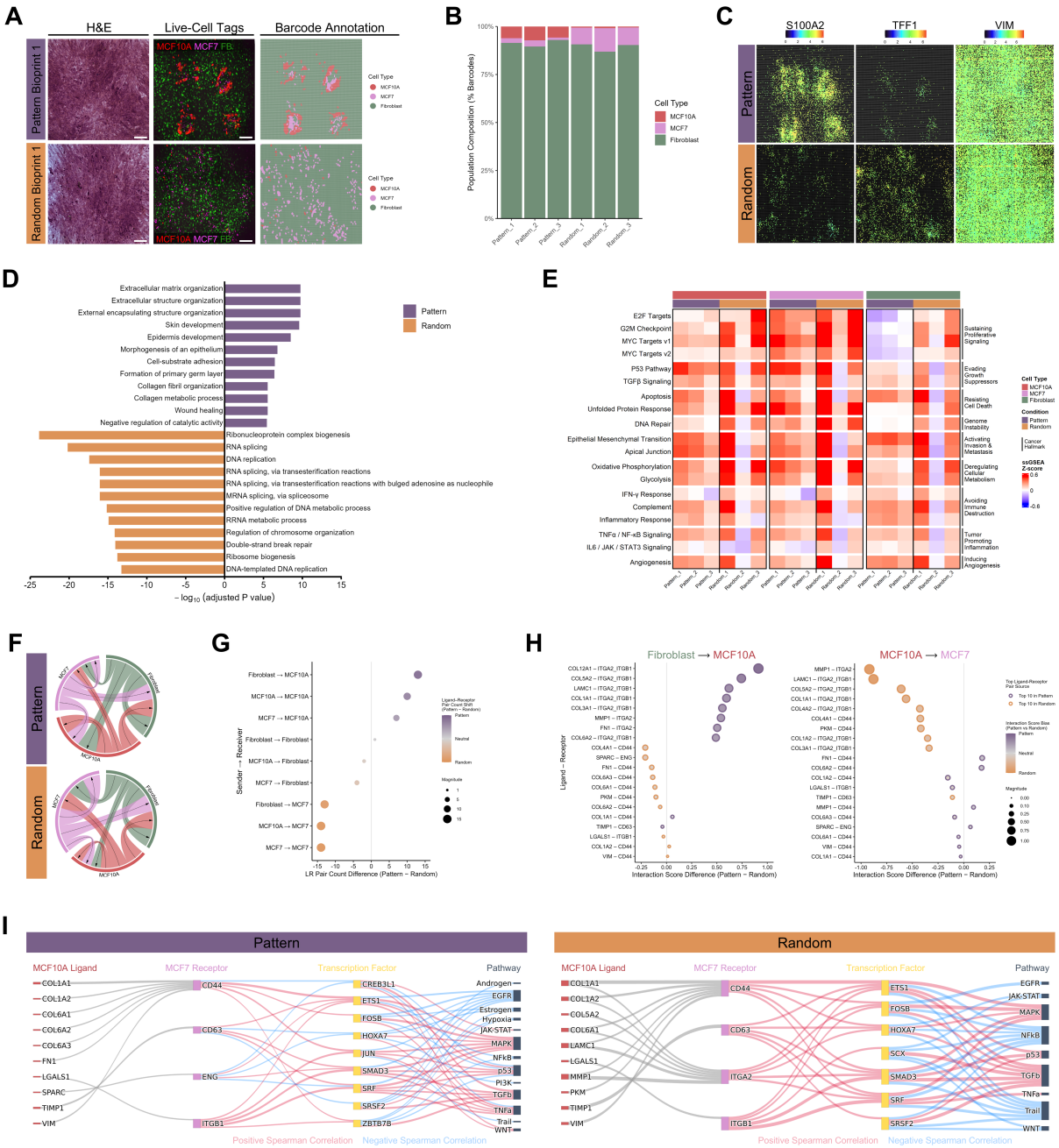

Figure 4. Spatial organization rewires gene expression, pathway activity, and signaling networks
(A) Representative images of pattern bioprint and random bioprint samples containing mammary epithelial cells (EF1α-tdTomato9+ MCF10A), breast cancer (H2B-iRFP+ MCF7), and mammary fibroblasts (H2B-mVenus+). H&E, live-cell image of fluorescently transduced cells, and barcode annotation.
(B) Proportion of spatial barcodes assigned to each cell type for each pattern or random bioprint replicate.
(C) Spatial expression of selected marker genes identified from single-population controls shown for pattern and random bioprints.
(D) Gene Ontology Biological Process (GO-BP) enrichment analysis of genes upregulated in patterned and random cultures, displayed as mirrored −log10(adjusted P value) following Benjamini–Hochberg correction.
(E) Single spot gene set enrichment (ssGSEA) Z-scores for selected MSigDB Hallmark cancer pathways.
(F) Ligand-receptor interaction networks. Edge weight represents ligand-receptor pairs.

(*legend continued on next page*)

(G) Change in ligand–receptor pair counts for each directed cell-type pair (Δ pairs = Pattern − Random). Color denotes directional shift (purple = pattern; orange = random) and point size indicates magnitude of change.
(H) Ligand–receptor interactions preferentially utilized under each spatial arrangement for select sender receiver interactions; fibroblast sender to MCF10A receiver (left) and MCF10A sender to MCF7 receiver (right). Point outline indicates whether the ligand-receptor pair came from the top 10 pairs in pattern bioprints (purple) or random bioprints (orange). Color reflects whether signaling was enriched in Pattern or Random and point size denotes the magnitude of change
(I) MCF10A to MCF7 ligand-receptor interactions, with inferred downstream transcription factor and pathway activities for pattern and random bioprints. Between ligand and receptor, edge width reflects inferred ligand-receptor interaction strength. Between receptor, transcription factor, and pathway nodes, edge widths indicate absolute Spearman correlation and color denotes Spearman sign (red = positive; blue = negative).

environmental influences rather than cell-type-intrinsic transcriptional programs (**Figure S8F-I**).

Given the pronounced transcriptional differences observed in identical starting cell types differing only in microscale spatial organization, we hypothesized that altered cell–cell signaling networks may underlie the divergent cell behaviors. Ligand–receptor inference using LIANA[33] provided evidence that spatial organization significantly reshaped intercellular communication networks (**Figure 4F–I**). Across all inferred cell–cell interactions, patterned and random configurations differed in predicted signaling directionality, with patterned constructs enriched for communication toward MCF10A and random organization favoring cancer-directed interactions (**Figure 4F–G**). Examination of individual predicted sender–receiver relationships further showed that spatial organization altered the specific ligand–receptor pairs preferentially mediating intercellular communication (**Figure 4H**). To contextualize how these ligand–receptor differences propagate downstream, we integrated ligand–receptor interactions with transcription factor[34,35] and pathway[36] inference (**Figure 4I**). Among the top inferred transcription factor–pathway couplings, MCF10A to MCF7 signaling in patterned organization was associated with positive coupling to WNT and JAK–STAT pathway activity in MCF7 cells. In contrast, random organization exhibited stronger negative coupling to TRAIL (TNF–related apoptosis-inducing ligand) and positive coupling to TGFβ pathway activity. Together, these analyses provide compelling evidence that spatial organization shapes cell–cell interactions and the structure of downstream signaling networks.

DISCUSSION

Here we report the development and optimization of a single-cell bioprinting approach that, for the first time, enables the direct replication of living tissue architectures at true single-cell resolution. Unlike existing in vitro models, which rely on stochastic self-organization or approximate tissue architecture at scales far larger than native tissues, our approach allows the deliberate placement of every individual cell with down to subcellular precision. Using this level of control, we show that changes in spatial arrangement alone are sufficient to drive divergent cellular behaviors, including distinct migratory trajectories, transcriptional states, and signaling programs.

Complex tissues such as the tumor microenvironment are characterized by rich cellular and spatial interactions, making causal relationships between structure and function difficult to resolve. Our platform overcomes this challenge by precisely controlling the position and spatial relationships of every cell, enabling systematic deconstruction of tissue architecture to determine how multicellular organization governs cell behavior. Unlike retrospective spatial-omics approaches, which capture organization at a single endpoint, this framework allows spatial configurations to be perturbed, monitored dynamically, and iterated over time. Treating spatial organization as an explicit, programmable parameter transforms spatial biology from descriptive association into prospective, mechanistic interrogation.

A key advance of this work is the integration of single-cell spatial transcriptomic analysis with engineered tissues fabricated at single-cell resolution. To achieve this, we adapted a whole-transcriptome, single-cell spatial transcriptomic workflow to be compatible with samples bioprinted directly onto microscope slides, bypassing embedding and sectioning to avoid sample loss or disruption.[37] This capability is particularly powerful because it allows every aspect of the tissue to be controlled: cell types, number, and position, the inclusion of fluorescent reporters for ground-truth validation or real-time monitoring, and live-cell imaging to capture dynamic behaviors. All measurements can then be directly linked to whole-transcriptome readouts, creating an unprecedentedly tractable system for connecting spatial context to molecular state. Our data from this pipeline demonstrate that the arrangement of cells dictates their dynamic interactions, signaling environments, and ultimately their transcriptional identities.

Consistent with this, transcriptomic analysis showed substantially greater biological variability across replicates in randomly deposited co-culture bioprints, where local cellular neighborhoods differ unpredictably due to stochastic mixing.

Together, these results represent a major advancement in biofabrication, achieving unprecedented resolution, heterogeneity, and faithful recapitulation of native cell–cell interactions. Agnostic to tissue type or disease, this bioprinting approach provides a generalizable framework for engineering complex microenvironments with single-cell precision and reproducible architecture. By linking controlled spatial organization to dynamic interactions, signaling states, and transcriptional identities, we provide both a conceptual and methodological foundation for dissecting how multicellular architecture governs biological function. Beyond technical innovation, single-cell bioprinting of entire tissue microenvironments to scale and with near-exact mimicry of cellular spatial organization opens a new chapter in spatial biology and biofabrication, enabling systematic construction and perturbation of heterogeneous tissue models to investigate development, disease progression, and therapeutic response at the level of individual cells. The potential implications for understanding and manipulating complex biological systems are broad, pointing toward new possibilities in new approach methodologies (NAMs) and mechanistic spatial biology.

Limitations of the study

Despite its capabilities, this platform has limitations. First, bioprinting success depends on cell–substrate adhesion, which can vary substantially across cell types and substrates. Highly adherent cells readily bind at the point of deposition, whereas weakly adherent or suspension cells are more difficult to pattern with the same reliability. While surface functionalization and post-bioprint encapsulation can mitigate this issue, these approaches can interfere with cell behavior and downstream assays. Second, the approach has limited throughput. Currently, achieving single-cell resolution requires manual control of the printhead and fluidics using a videogame-like controller with real-time visual confirmation. This is because existing microfluidic cell-dispensing systems, including the one used in this study, lack integrated sensing for fully automated closed-loop control. This tradeoff prioritizes spatial accuracy over speed thus limiting scalability.

Finally, although we demonstrate the ability to pattern single cells in 3D, the models presented here are primarily planar and therefore do not capture higher-order three-dimensional features of native tissues, including cell-cell and cell-ECM interactions in the Z plane. Extending this approach to 3D constructs, while maintaining single-cell spatial fidelity, remains an active direction of our future work.

RESOURCE AVAILABILITY

Lead contact

Further information and requests should be directed to and will be fulfilled by the lead contact, Luiz E. Bertassoni (bertasso@ohsu.edu).

Materials availability

Printer modifications have been made available free of charge on GitHub: https://github.com/ware-research/heater_feedback_controller/tree/v1.1 and https://github.com/ware-research/transparency_overlay/tree/v.1.1.

Data and code availability

The spatial transcriptomic dataset generated during this study has been deposited in the National Center for Biotechnology Information (NCBI) Gene Expression Omnibus and is accessible through GEO Series accession number GSE315233: https://www.ncbi.nlm.nih.gov/geo/query/acc.cgi?acc=GSE315233. The code used to analyze the cell-cell interaction arrays and spatial transcriptomics data is available at: https://github.com/HaylieHelms/2DscBioprinting2 and has also been deposited at Zenodo: https://zenodo.org/records/18563242. Any additional information required to reanalyze the data reported in this paper is available from the lead contact upon request.

ACKNOWLEDGEMENTS

The authors thank Michael McLellan of Christopher Chen's lab for generating the hiPSC derived cardiomyocytes, Ryan Gordon for sharing the prostate cancer cell line PC3, Jens Kreth for sharing the monocyte cell line THP-1, Avathamsa Athirasala for generating the transduced MCF10A cell line, Rawan Makkawi for their collaboration to generate the

histone 2B lentiviral reporters used to transduce the MCF7, MDA-MB-231 and fibroblasts, and Jason Ware for building the printer modifications. This work was supported by funding from the Cancer Early Detection Advanced Research Center, Knight Cancer Institute, Oregon Health and Science University (Full 2023-1745) awarded to H.R.H. and L.E.B, OHSU Silver Family Innovation Award awarded to L.E.B, and the M.J. Murdock Charitable Trust. Institutional support was provided by the OHSU Knight Cancer Institute NCI Cancer Center Support Grant (P30CA069533) for the Advanced Light Microscopy Core (RRID:SCR_009961). L.E.B. also acknowledges support from the National Institute of Dental and Craniofacial Research (R01DE035326), Knight Cancer Institute Pilot Award, and Cancer Early Detection Advanced Research Center (Full 2023-1719). H.R.H. acknowledges support from the International Alliance for Cancer Early Detection (ACED) PhD Fellowship and Achievement Rewards for College Scientists (ARCS) Foundation Oregon. A.E.D. acknowledges support from National Institutes of Health, Office of Research Infrastructure Programs (K01OD031811). E.M.L. acknowledges support from a Research Scholar Grant (RSG-22-060-01-MM) from the American Cancer Society (https:doi.org/10.53354/pc.gr.153686) and an ACED Project Award (ACNCR1743). The authors also thank the Cell, Developmental and Cancer Biology Summer Research Internship program at the Knight Cancer Institute, Oregon Health and Science University for supporting K.A.O. The International Alliance for Cancer Early Detection (ACED) is a partnership between Cancer Research UK, Dana Farber Cancer Institute, The University of Manchester, the German Cancer Research Center (DKFZ), University College London, Knight Cancer Institute at OHSU, and The University of Cambridge.

AUTHOR CONTRIBUTIONS

H.R.H. designed the research with L.E.B; acquired funding; conceptualized printer modifications; performed the experiments; developed the spatial transcriptomics assay modifications; analyzed the data; and wrote the manuscript. K.A.O. worked with H.R.H. to create the patient matched bioprint map, assisted during bioprinting, and contributed to cell tracking. A.E.D. and E.M.L advised experimental design and imaging; and reviewed and edited the manuscript. L.E.B. conceived the research; acquired funding; supervised the work; and edited the manuscript.

DECLARATION OF INTERESTS

L.E.B is a co-founder of and has an equity interest in RegendoDent Inc. L.E.B is named on patents that have been licensed by RegendoDent Inc. His interests were reviewed and managed in accordance with the OHSU institutional conflict of interest policies. E.M.L. is an inventor on bioprinting technology that has been optioned to Organovo, Inc. by OHSU. This potential conflict of interest has been reviewed and managed by OHSU.

EXPERIMENTAL MODEL DETAILS

Human cell culture

All cells were cultured at standard 37ºC and 5% CO_2. Unless otherwise stated, media was changed every 2-3 days and cells were passaged at 70% confluency using TrypLE Express (Gibco).

Primary cultures

Green fluorescent protein-expressing human umbilical vein endothelial cells (GFP-HUVEC, Angio-proteomie) were cultured in vascular endothelial growth factor endothelial growth medium (VascuLife VEGF, Lifeline Cell Technology). Bone marrow-derived mesenchymal stem cells (MSC, RoosterBio) were cultured in alphaMEM (Gibco) supplemented with 10% MSC-qualified fetal bovine serum (FBS, Gibco) and 1% penicillin-streptomycin (Gibco). Mammary fibroblasts (ScienCell) were cultured in DMEM (Gibco) supplemented with 10% FBS and 1% penicillin-streptomycin. Osteoblasts (ATCC) were cultured in osteoblast growth medium (Cell Applications). Macrophages (Celprogen) were cultured in human macrophage cell culture medium with serum (Celprogen). Human myoepithelial cells were isolated from reduction mammoplasty tissue[38] (Dr. William C. Hines lab, University of New Mexico) and cultured on a type I bovine collagen coating (PureCol, 100 µg/mL working concentration, Advanced Biomatrix) in M87 media. M87 media is a 1:1 mixture of Medium 171 (Gibco) and DMEM/F-12 (Gibco) supplemented with 0.25% FBS, 2mM L-glutamine (Gibco), 0.1% w/v Albumax (Gibco), 35 µg/mL bovine pituitary extract (Gibco), 5 ng/mL epidermal growth factor (PeproTech), 0.3 µg/mL hydrocortisone (Sigma), 0.5 ng/mL cholera toxin (Sigma),

7.5 μg/mL insulin (Sigma), 2.5 μg/mL apo-transferrin (Sigma), 0.1 nM oxytocin acetate salt (Sigma), 0.5 nM β-estradiol (Sigma), 5 nM Tri-iodothyronine (Sigma), and 5 μM isoproterenol (Sigma).

Cell lines

MDA-MB-231 (ATCC), MCF7 (Horizon Discovery), and SH-SY5Y (ATCC) were cultured in DMEM (Gibco) supplemented with 10% FBS and 1% penicillin-streptomycin. PC3 (ATCC) and THP-1 (ATCC) were cultured in RPMI 1640 supplemented with 10% FBS and 1% penicillin-streptomycin. MCF10A (Horizon Discovery) were cultured in DMEM/F12 (Gibco) supplemented with 5% horse serum (Gibco), 20 ng/mL epidermal growth factor (PeproTech), 0.5 mg/mL hydrocortisone (Sigma), 100 ng/mL cholera toxin (Sigma), 10 μg/mL insulin (Sigma), and 1% penicillin-streptomycin.

Differentiation

THP-1 derived macrophages were generated following a previously established protocol.[39] Briefly, THP-1 were seeded into a 6 well plate at 2 x 10^5 cells/well and treated with 20 ng/mL phorbol-12-myristate 13-acetate (PMA, Sigma) in RPMI 1640 supplemented with 10% FBS. The media containing PMA was removed after 24 hours and cells were allowed to rest in fresh RPMI without PMA for 24 hours prior to use. Cardiomyocytes, kindly provided by Dr. Christopher S. Chen's lab, were derived from human induced pluripotent stem cells (hiPSCs) via small molecule manipulation of the Wnt signaling pathway.[40,41] Cardiomyocytes were cultured on Matrigel coated plates in RPMI supplemented with 1:50 B-27 (Fisher) and 5% FBS. The culture was maintained until the cardiomyocytes resumed beating before harvesting for bioprinting.

METHOD DETAILS

Cell preparation for single-cell bioprinting

Cells were detached using TrypLE express for the minimum possible time and pelleted at 300 g for 3-5 minutes. While bioprinting can be done label free, cells were either transduced to include a fluorescent reporter (iRFP or mVenus Histone 2B or tdTomato-9 EF1α (Takara Bio)) or fluorescently tagged using Hoechst (NucBlue Live ReadyProbes,

Invitrogen) or general membrane cell tracker (Cellvue Claret Far Red, PKH26 Red Fluorescent Cell Linker, or PKH67 Green Fluorescent Cell Linker, Sigma) following the manufacturer's protocol to facilitate downstream analysis. Cells were then resuspended at 1 x 10^6 cells/mL in a 1:1 mixture of complete cell culture medium and polyethylene glycol (PEG, 35,000 m.w., 30 mg/mL, Sigma).

Biopixlar modifications

The microfluidic dispenser (Biopixlar, Fluicell, Mölndal, Sweden) configuration was adjusted so that the printhead was angled at 70º and retrofitted with a heating unit to maintain the chamber at 37 °C.[42] A custom transparency overlay software was also developed to facilitate high precision patterning.[28]

Heating unit

Two 110 V, 100 W, 3.66 by 0.94 by 1.18 inch, ceramic air heater cartridges were used (ASIN: B01COPT7BG). A temperature control unit (model ITC-106VH) and solid state relay module (model SSR-40 DA) were purchased from Inkbird Tech C.L.. The temperature control unit and solid-state relay module were wired according to the documentation provided with the modules. Two ceramic heater cartridges were wired in parallel to the output of the solid-state relay module. The thermocouple was mounted onto the Biopixlar printhead holder near the tip and the heating modules were positioned on adjustable arms approximately 15 cm from the printing area. The controller was set to heat mode, with a threshold temperature of 37 °C, a control period of 4 seconds, a proportional band term of 30, an integration time of 30 seconds, and a derivative time of 8 seconds. Available at: https://github.com/ware-research/heater_feedback_controller/tree/v1.1

Bioprint map transparency overlay

A custom python program (Python v. 3.10.0) was developed to overlay a transparent image of the target bioprint map over the live microscope feed of the Biopixlar software.[28] The software has been made available free of charge and can be accessed at: https://github.com/ware-research/transparency_overlay/tree/v.1.1

General single-cell bioprinting setup

A 1.5 mg/mL collagen I (Gibco) receiving substrate was prepared by adding 200 µL of collagen to the inner ring of a 35 mm, low walled petri dish (µ-Dish 35 mm low, Ibidi) and placed in the incubator for 30 minutes to crosslink. A 30 µm channeled PDMS printhead (FBPX-30, Fluicell) was primed by adding 25 µL of ultra-pure sterile water (Invitrogen) to each well of the printhead and inserted into the priming pump (Fluicell) at 180 mbar for 3 minutes. Immediately prior to bioprinting, the water was removed from all waste collection wells and any wells which cells will be added to 25 µL of each cell suspension (1 x 10^6 cells/mL in a 1:1 mixture of complete cell culture medium and 35,000 m.w. polyethylene glycol at 30 mg/mL) was added to the desired delivery wells. The printhead was loaded into the Biopixlar and prime 1 pre-set was executed (180 mbar delivery pressure to wells 1-4 simultaneously). 1.5 mL complete medium was added to the 35 mm dish containing the crosslinked collagen substrate and loaded into the printer. Following the completion of prime 1, the tip was gently wiped with the provided lint-free cloth (Fluicell) before lowering the printhead into the dish. Prime 2 pre-set was then executed to remove any bubbles in the fluidics (-220 mbar external and internal vacuums). The print surface was identified by dispensing a few cells onto the surface, bringing them into focus with the onboard microscope (LS620, Etaluma), and lowering the printhead next to the attached cells until a slight deflection was observed. If cells weren't binding, the printhead was lowered at 5 µm increments. The cells used to identify the surface were removed by increasing the internal vacuum and aligning the dispensing channel with the cells. Bioprints were visualized in real-time during bioprinting using the onboard microscope (LS620, Etaluma). Fluorescent images of live cells, pre-labeled with a fluorescent tag prior to bioprinting, were acquired using either EVOS Fl Auto Imaging System (Life Technologies) or spinning disk confocal (Yokogawa CSU-X1 on Zeiss Axio Observer).

Recirculation zone stability assessment

To assess the stability of the recirculation zone, fluorescein (200 µM in 1x PBS) was added into well 1 of the printhead and 1x PBS was added to wells 2-4. The printhead was lowered into a petri dish containing 1x PBS and a collagen substrate. Delivery pressure was set to either 60, 80, or 100 mbar, with non-delivery set to 0 mbar, and the internal

and external vacuum settings were varied at 10 mbar increments from 0 to -100 mbar. The delivery pressure was applied for 10 seconds to observe the stability of the recirculation zone. If the area of the recirculation zone didn't expand over the 10 second period, the recirculation was considered stable. A snapshot was taken at the 10 second mark before stopping the delivery pressure. This process was repeated across three different printheads (FBPX-30, Fluicell) to assess printhead-to-printhead variability.

Maximum internal vacuum assessment

GFP-HUVECs were added to well 1 and 1x PBS was added to wells 2-4. The delivery pressure was set to either 60, 80, or 100 mbar with equal external vacuum and 0 mbar non-delivery pressure. The internal vacuum was varied at 10 mbar increments from 0 to -50 mbar to determine the range of internal vacuum settings that support cell dispensing. The delivery pressure of the cell containing well was applied for 10 seconds and cell dispensing (yes/no) was recorded. This process was repeated across three different printheads (FBPX-30, Fluicell), with n = 3 per printhead, to assess printhead-to-printhead variability.

Minimum internal vacuum assessment

GFP-HUVECs were added to well 1 and GFP-HUVECs co-tagged with Hoechst (NucBlue Live ReadyProbes, Invitrogen) were added to wells 2-4. Delivery pressure was set to either 60, 80, or 100 mbar, with equal external vacuum and 0 mbar non-delivery pressure, and the internal vacuum was varied at 10 mbar increments from 0 to -40 mbar. GFP-HUVECs in well 1 were dispensed in a straight line for 10 seconds. If a Hoechst + GFP-HUVEC was dispensed, the internal vacuum setting was determined to be too low. This process was repeated across three different printheads (FBPX-30, Fluicell), with n = 3 per printhead, to assess printhead-to-printhead variability.

Optimized single-cell bioprinting settings

Regardless of cell type, 1 x 10^6 cells/mL in a 1:1 mixture of complete cell culture medium and polyethylene glycol (PEG, 35,000 m.w., 30 mg/mL) was found to be suitable for single-cell deposition and binding onto a 1.5 mg/mL collagen I substrate. Optimized flow

settings were 80 mbar delivery, 0 mbar non-delivery, -25 mbar internal vacuum, and -40 mbar external vacuum. For bioprints with cells positioned less than 25 µm away from one another, the external vacuum was dropped as low as -25 mbar to avoid disrupting the freshly deposited cells.

Alternative receiving substrates

35 mm, low walled petri dishes (µ-Dish 35 mm low Grid-500, Ibidi) were prepared by coating the surface with one of the following materials: 0.1% w/v gelatin (from porcine skin, gel strength 300 Type A, Sigma) in sterile water and incubated at room temperature for 5 minutes, Matrigel (Corning) diluted 1:80 in DMEM/F12 and incubated at 37 °C for 1 hour, or 2 µg/mL Poly-L-Lysine (PLL, ScienCell) in sterile water and incubated at 37 °C for 1 hour. Excess solution was aspirated and replaced with 1.5 mL of the cells complete medium minus FBS. PLL coated dishes require two washes with sterile water before the addition of cell culture medium. To create three-dimensional stacks of collagen, the complete medium was aspirated from the dish following the completion of bioprinting. An additional 25 uL of collagen I was gently pipetted onto the surface and incubated at 37 °C and 5% CO_2 for 15 minutes. Fresh medium was added to the dish and the bioprinting resumed on the new layer of collagen.

Cell-cell interaction arrays

Arrays of varied cell arrangement

MDA-MB-231 were stained with PKH26 Red Fluorescent Cell Linker (Sigma, Cat # PKH26GL) for general cell membrane labeling prior to bioprinting. GFP+ HUVEC and MDA-MB-231 were bioprinted in a 4 x 4 array with each bioprint containing equal number of each cell type (8 HUVEC and 8 MDA-MB-231) and 100 µm spacing between each cell. The spatial arrangement of the cells was either segregated (like cell types grouped half and half, 2x4), clustered (like cell types clusters in the corners, 2x2), or mixed (alternating cell types) to investigate the effect of spatial patterning on cell behavior. Bioprints were cultured in a 1:1 mixture of HUVEC complete medium and MDA-MB-231 complete medium. Once bioprinting was complete, samples were live-cell imaged on a spinning

disk confocal (Yokogawa CSU-X1 on a Zeiss Axio Observer) with environment chamber at 37 °C and 5% CO_2. Images were taken with fixed intervals of 10 minutes over 30 hours.

Arrays of varied cell composition

H2B-iRFP+ MDA-MB-231 were bioprinted in a 4 x 4 array of cells, with 100 µm spacing between each cell, either alone or in mixed (alternating configuration) with either myoepithelial cells, mammary fibroblasts, or macrophages (all human primary). Bioprints were cultured in M87 media and imaged at fixed intervals of 10 minutes for 24 hours on a spinning disk confocal (CrestOptics X-Light V3 on a Nikon Ti2) with environment chamber set at 35 °C and 5% CO_2.

Breast cancer biopsy recreation

To replicate a tumor biopsy region of interest, a breast cancer biopsy previously annotated using imaging mass cytometry was selected.[29] A region containing a breast duct with surrounding stroma was selected and imported into ImageJ. The image was converted to an 8-bit image and threshold to segment each cell. Cells that were incorrectly fused were manually separated by drawing an eraser line. The particles were then analyzed and any cell with an area less than 254.47 μm^2 (18 µm diameter, ~the average size of our detached cells) was removed. The resulting masked image was manually re-colored using Procreate (Savage Interactive) to return the annotations. A 3D bioprint map model was then created using Fusion 360 (Autodesk CAD) by placing 18 µm diameter spheres in the center of each cell of the mask. In regions where cells had been removed due to size limitation, spheres were evenly distributed to fill in the void. The resulting 3D model was exported as the bioprint map with the X,Y location of each cell. Using our custom overlay software[28], the bioprint map was matched using MCF10A, MDA-MB-231, mammary fibroblasts, mesenchymal stem/stromal cells, and THP-1 derived macrophages. The bioprint was cultured in a 1:6 mixture of MCF10A media and DMEM supplemented with 10% FBS and 1% penicillin-streptomycin. Live-cell imaging was conducted using a widefield fluorescent microscope (Nikon Ti2), acquiring an image every 10 minutes over 24 hours, with environment chamber at 37 °C and 5% CO_2.

Breast tumor microenvironment model

A pre-invasive breast cancer model was fabricated by first bioprinting 200 μm diameter rings of MCF10A onto a collagen substrate in M87 medium. The bioprints were returned to the incubator while the remaining cell types were harvested. MDA-MB-231 or MCF7 were deposited within the MCF10A ring and primary mammary fibroblasts were patterned around the MCF10A rings and throughout the stromal compartment. A thick fibroblast box "wall" was bioprinted around the entire bioprint to serve as physical boundaries to promote cells staying within the region instead of migrating to fill in the vast open spaces of the 35 mm petri dish. To simulate standard co-culture approaches, MCF10A, MDA-MB-231 or MCF7, and mammary fibroblasts were mixed at a 2:1:5 ratio respectively and loaded into a single well of the printhead. Cells were deposited in a random distribution, and no box perimeter was bioprinted. Immediately following bioprinting, live-cell imaging began on a widefield fluorescent microscope (Nikon Ti2) with environment maintained at 37 °C and 5% CO_2. Images were acquired every 10 minutes for 24 hours.

Immunostaining

Bioprints were washed three times with 1x PBS and fixed using 10% neutral buffered formalin (Thermo Fisher) for 30 minutes at room temperature. Cells were permeabilized using 0.1% Triton X-100 (Sigma) solution in PBS for 15 minutes at room temperature. The samples were then blocked using 1.5% bovine serum albumin (BSA, Sigma) in PBS for 1 hour at room temperature. Primary antibodies pan cytokeratin (PanCK, 1:100, OriGene) and vimentin (VIM, 1:200, Novus Biologicals) were added in 0.15% BSA and incubated at 4 °C overnight. Primary antibodies were removed, and the samples were washed three times with PBS before adding secondary antibodies (goat anti-mouse Alexa Fluor 555 and goat anti-rabbit Alexa Fluor 647, 1:250). Secondary antibodies were incubated at room temperature for 2 hours, removed, and samples washed twice with 0.1% Tween 20 (Fisher Biotech). Nuclei were labeled with DAPI (NucBlue Fixed Cell ReadyProbes, Invitrogen) in PBS for 30 minutes at room temperature. Samples were then imaged using a spinning disk confocal (Yokogawa CSU-X1 on Zeiss Axio Observer).

Spatial transcriptomics

The Visium HD Spatial Gene Expression assay (10x Genomics, Human Transcriptome, 6.5 mm) was modified as we previously reported[37] to enable analysis of planar cell cultures without sectioning and embedding. Briefly, a standard microscope glass slide was sterilized in 70% ethanol, rinsed with ultrapure sterile water, and coated with type I bovine collagen solution (PureCol, 100 µg/mL working concentration, Advanced Biomatrix). Cells were bioprinted directly onto the treated slide submerged in M87 medium to create the following groups: patterned tumor microenvironment, randomly deposited co-culture, and single population controls. The patterned samples were created by bioprinting four tdTomato9-EF1α+ MCF10A rings (200 µm in diameter), with H2B-iRFP+ MCF7 bioprinted in the center and H2B-mVenus+ mammary fibroblasts surrounding the rings. Random samples were fabricated by mixing the same ratio of cells as the patterned sample (1:2:5 MCF7:MCF10A:FB), loading into a single well of the printhead, and depositing over an equivalent area and density as the patterned samples. Single cell type controls were bioprinted onto one of the capture areas to serve as internal references. Samples were cultured for 24 hours. Immediately prior to fixation, a fluorescent image was taken to serve as a ground truth cell type identifier, as each cell type was transduced with a unique fluorescent reporter. Samples were then fixed with 4% paraformaldehyde (PFA) for 30 minutes at room temperature and permeabilized in 100% methanol on ice for 1 hour. H&E staining, imaging, destaining, and decrosslinking were performed according to the Visium HD FFPE Tissue Preparation Handbook (CG000684, Rev A). The manufacturer's protocol (Visium HD Spatial Gene Expression User Guide CG000685, Rev B) was followed thereafter to generate the spatial gene expression libraries. The library was sequenced by NovoGene on an Illumina NovaSeq X Plus with a depth of approximately 400 million reads per sample. FASTQ files, H&E images, and spatial metadata were processed using Space Ranger v3.1.3 with the GRCh38-2020-A human reference genome and Visium human transcriptome probe set v2.0.

QUANTIFICATION AND STATISTICAL ANALYSIS

Cell motion tracking, quantification, and analysis

Motion tracks were manually created in Imaris (Oxford Instruments, Version 10.2) by clicking the center of each cell per frame. Tracks were split when a cell division occurred and the daughter cell's track began at the first frame it was visible. Raw x and y coordinates were exported for analysis.

Total distance traveled and normalized distance

Total distance traveled was calculated for each cell trajectory by summing the Euclidean distance between consecutive frames:

$$L_n = \sum_{t=1}^{T_n - 1} \sqrt{\left(x_{n,t+1} - x_{n,t}\right)^2 + \left(y_{n,t+1} - y_{n,t}\right)^2}$$

Where T_n is the number of valid frames for cell n, and $\left(x_{n,t}\,,\, y_{n,t}\right)$ are the raw x, y coordinates at frame t.

To account for cells that traveled out of the field of view or divided, which would truncate track length sums, we normalized distanced traveled by the number of consecutive frames observed:

$$D_n = \frac{L_n}{T_n - 1}$$

Where D_n is the distance traveled per visible frame for cell n, and $(T_n - 1)$ is the number of consecutive frame intervals over which the cell was observed.

Mean squared displacement

The time averaged mean squared displacement (TASD)[43] was calculated for each cell trajectory using the following equation:

$$\langle r_n^2(\tau)\rangle_t = \langle\left[r_{x,n}(t+\tau) - r_{x,n}(t)\right]^2 + \left[r_{y,n}(t+\tau) - r_{y,n}(t)\right]^2\rangle_t$$

Where $r_{x,n}(t)$ and $r_{y,n}(t)$ are the x and y coordinates of cell n at time t, and $\langle\cdot\rangle_t$ denotes the average taken over all time points for which a corresponding position at $t + \tau$ exists. Cells were imaged at fixed interval Δt, so lag times occurred at discrete steps $\tau = k\Delta t$,

where k is the lag in frames. TASD values $\langle r_n^2(\tau)\rangle_t$ were computed for each cell and then averaged across all cells belonging to a given experimental group. The standard error of the mean (SEM) at each τ was calculated across cells contributing measurements at that lag.

To assess how cell migration scaled over time, we examined the power-law relationship[43]

$$TASD(\tau) \propto \tau^{\alpha}$$

Where α is the anomalous diffusion exponent describing the mode of migration. Subdiffusive motion $(0 \leq \alpha < 1)$ reflects restricted or confined movement, $\alpha = 1$ corresponds to Brownian (random) motion, and $\alpha > 1$ indicates superdiffusive or persistent migration. For each cell type and spatial arrangement, α was extracted by fitting the linearized form:

$$\log\big(TASD(\tau)\big) = \beta_0 + \alpha \log(\tau)$$

Only finite TASD values greater than zero were retained, TASD values within a defined lag-time window of 50-500 minutes were used, and a minimum of three points was required for a valid fit. The slope of the regression yielded α, and the coefficient of determination (R^2) was used to assess the quality of the fit.

Net displacement

Net displacement for each cell was calculated using the following equation:

$$D_n = \sqrt{\left(x_{n,final} - x_{n,initial}\right)^2 + \left(y_{n,final} - y_{n,initial}\right)^2}$$

Where $\left(x_{n,initial}\,,\ y_{n,initial}\right)$ is cell the starting position of cell n and $\left(x_{n,final}\,,\ y_{n,final}\right)$ is the final position of that cell.

Center of mass displacement

The center of mass (COM) of the HUVEC population was calculated separately for each bioprinted array by averaging the x and y coordinates of all tracked cells. For each replicate at time t, COM was defined as:

$$COM_x(t) = \frac{1}{N_t}\sum_{i=1}^{N_t} x_i(t)$$

$$COM_y(t) = \frac{1}{N_t}\sum_{i=1}^{N_t} y_i(t)$$

Where N_t is the number of cells contributing positional measurements at time t. To quantify population-level shifts over time, COM trajectories were centered such that the initial position served as the origin:

$$\Delta X(t) = COM_x(t) - COM_x(t_0)$$
$$\Delta Y(t) = COM_y(t) - COM_y(t_0)$$

For each spatial arrangement, $\Delta X(t)$ and $\Delta Y(t)$ curves were averaged across independent bioprinted arrays (three arrays per arrangement), and the standard error of the mean (SEM) was calculated at each time point. For each array, a time averaged COM displacement was then calculated along X and Y by averaging $\Delta X(t)$ and $\Delta Y(t)$ over the full 30 hour imaging period.

Distance to nearest neighbor

For each MDA-MB-23, the distance to its nearest non-MDA-MB-231 neighbor was computed:

$$d_{n,m}(t) = \sqrt{\left(x_{n,t} - x_{m,t}\right)^2 + \left(y_{n,t} - y_{m,t}\right)^2}$$

Where $\left(x_{n,t}, y_{n,t}\right)$ are the coordinates of MDA-MB-231 cell n and $\left(x_{m,t}, y_{m,t}\right)$ are the coordinates of non-MDA-MB-231 cell m in the same time frame t.The nearest neighbor distance for cell n was then defined as:

$$d_n(t) = \min_m d_{n,m}(t)$$

For each experimental group (TNBC + Myoepithelial, TNBC + Fibroblast, or TNBC + Macrophage) and time point, nearest neighbor distances were averaged across all MDA-MB-231 (TNBC) cells:

$$\overline{d_g}(t) = \frac{1}{N_{g,t}}\sum_{n=1}^{N_{g,t}} d_n(t)$$

Where g is the experimental group, $\overline{d_g}(t)$ is the mean nearest neighbor distance at time t, and $N_{g,t}$ is the number of MDA-MB-231 cells contributing measurements.

Migration territory

To quantify the two-dimensional territory explored by migrating cells, trajectories were first translated so that each track began at the origin. For each cell n, raw coordinates $(x_{(n,t)}, y_{(n,t)})$ were converted to relative coordinates

$$RelX_{(n,t)} = x_{(n,t)} - x_{(n,0)}, \qquad RelY_{(n,t)} = y_{(n,t)} - y_{(n,0)}$$

such that $\left(RelX_{(n,0)}, RelY_{(n,0)}\right) = (0,0)$.

For each sample, the minimal convex polygon enclosing all relative positions of the cell type of interest was computed using the Quickhull algorithm (convhulln, geometry package). Given an ordered set of K_n hull vertices i for cell n, with the polygon closed by $\left(x_{(n,K_n+1)}, y_{(n,K_n+1)}\right) = \left(x_{(n,1)}, y_{(n,1)}\right)$, the migration territory was defined by the area of the convex hull:

$$A_n = \frac{1}{2}\left|\sum_{i=1}^{K_n}\left(x_{(n,i)}y_{(n,i+1)} - x_{(n,i+1)}y_{(n,i)}\right)\right|$$

Biopsy replica bioprint fidelity analysis

The fluorescence image of the resulting bioprints were imported into Fusion360 (Autodesk CAD). 18 µm diameter spheres were placed in the center of each cell of the image, following the same approach used to generate the print map. Fidelity analysis was performed using one full-field image of the biopsy replica and three smaller subregions sampled from three additional prints. The resulting 3D models of the bioprints and the original bioprint map 3D model were exported as .OBJ files and imported into CloudCompare (v2.13.2). A cloud to mesh (C2M) distance comparison was computed using the default settings (octree level: auto; absolute distances). The points were visualized with a histogram, and a Gaussian distribution was fitted to determine bioprint fidelity. Values reported as average ± standard deviation.

Spatial transcriptomics data processing

Space Ranger outputs for each Visium HD capture area were imported into R (v4.4.2) using the Load10X_Spatial function in Seurat (v5) at an 8 µm bin size, and each object

was assigned a unique capture area identifier. Custom metadata were curated using Loupe Browser (10x Genomics, v8) as previously described.[37] Because the versions of Loupe Browser and Space Ranger available at the time of experimentation did not allow for the simultaneous alignment and processing of an IF image and an H&E image, our custom transparency overlay software[28] was used to superimpose the fluorescent image of each sample taken right before fixation onto the Loupe Browser image. The custom group and paintbrush tools in Loupe were then used to manually annotate each barcode based on the fluorescence and cell morphology (H2B-iRFP+ MCF7, tdTomato9-EF1α+ MCF10A, and H2B-mVenus+ mammary fibroblasts). The annotated barcodes were exported as a .csv file and integrated into the Seurat object metadata. The custom group and rectangle selection tool in Loupe Browser was also used to assign sample ID and condition (Print Pattern) to each barcode. Datasets from the two capture areas were then merged, and Raw counts were log-normalized (LogNormalize, scale factor = 10,000) to generate the normalized data layer used for downstream analyses.

Gene ontology

For pathway-level comparisons between patterned and random cultures, barcodes belonging to each bioprint replicate were aggregated, and differential expression was performed between Pattern and Random conditions in Seurat (Wilcoxon test, Benjamini–Hochberg correction). Genes significantly upregulated in each condition (adjusted $P < 0.05$) were converted to Entrez IDs and analyzed using clusterProfiler[44] for Gene Ontology Biological Process over-representation (enrichGO, OrgDb = org.Hs.eg.db, ontology = “BP”). The top enriched terms for Pattern and Random were visualized as mirrored −log10(adjusted P) bar plots.

Single-spot gene set enrichment analysis (ssGSEA)

To quantify pathway activity at single-spot resolution, we performed ssGSEA using the Escape[45] (runEscape, method = “ssGSEA”) on log-normalized expression values. Cancer hallmark[32] gene sets (MSigDB collection H) were retrieved via msigdbr[46,47], and a curated panel of 19 cancer-relevant pathways (E2F targets, G2M checkpoint, MYC targets v1 and v2, P53, TGFβ signaling, apoptosis, unfolded protein response, DNA repair, epithelial

mesenchymal transition, apical junction, oxidative phosphorylation, glycolysis, interferon gamma response, complement, inflammatory response, TNFα via NF-κB, IL6–JAK–STAT3 signaling, and angiogenesis) were used for scoring. ssGSEA scores were computed independently for each spatial barcode, z-scaled across the dataset, and aggregated within each cell line (MCF10A, MCF7, fibroblast) and culture condition (Pattern, Random, Control). Differences in pathway activity were evaluated using Wilcoxon rank-sum tests, including comparisons to mono-culture controls.

Ligand-receptor analysis

Ligand–receptor interactions were inferred using LIANA[33,48] (version 1.6.1; Python) with the rank_aggregate framework and consensus ligand-receptor resource. Cell type barcode annotations were used to define sender and receiver populations, and interactions were filtered using an expression proportion threshold of 0.1 with 1,000 permutations (remaining parameters default). Ranked interaction outputs were exported for downstream visualization in R. For display, rank-based LIANA metrics were transformed such that higher values indicate stronger or more specific interactions (e.g., 1 − magnitude_rank and 1 − specificity_rank).

To evaluate how cell–cell signaling differed between spatial arrangements, ligand–receptor results were aggregated by sender–receiver pair to construct directed signaling networks for Pattern and Random bioprints. Networks were visualized as chord diagrams (Circlize[49]; R), with edge weights corresponding to the number of ligand–receptor pairs connecting each source–target pair. Sender–receiver rewiring was quantified by computing the change in ligand–receptor pair counts for each directed cell-type pair (Δ pairs = Pattern − Random) and visualized as a dot plot, with color encoding the directionality of rewiring and point size indicating its magnitude.

To assess changes at the level of individual signaling interactions, we examined the highest-ranked ligand–receptor pairs within selected sender–receiver interactions by comparing condition-specific LIANA interaction scores. For each directed cell-type pair, non-overlapping top-ranked ligand–receptor pairs in Pattern and Random configurations were identified and visualized based on the difference in interaction strength (Pattern −

Random), highlighting ligand–receptor interactions preferentially utilized under each spatial arrangement.

To link inferred cell–cell communication with downstream regulatory programs in receiver populations, ligand–receptor interactions identified by LIANA were integrated with transcription factor and pathway activity inference using decoupler[34] (version 2.1.2; Python). For each sender–receiver cell type pair, TF activities in the receiver cells were estimated from gene expression using the CollecTRI[35] regulatory network and the ULM method, while pathway activities were inferred using the PROGENy[36] model and the MLM method (human, top 100 target genes per pathway). Receptor–TF and TF–pathway associations were defined by Spearman correlation across receiver cells, and network edge weights were normalized across spatial conditions to enable direct comparison of inferred signaling architectures.

Statistical analysis

Cell migration and spatial organization metrics, including distance traveled, normalized distance, net displacement, center-of-mass displacement, convex hull area, and confinement index, were compared across experimental conditions using one-way ANOVA with Tukey's correction for multiple comparisons when three groups were analyzed (Segregated, Clustered, Mixed). For comparisons involving four microenvironment composition conditions (TNBC, TNBC+Myoep, TNBC+FB, TNBC+Mac), global differences were assessed using Welch's one-way ANOVA to account for unequal variances, followed by pairwise Welch t-tests with Benjamini–Hochberg correction. Data are shown as individual observations with violin/boxplot overlays at the per-cell or per-track level, and as mean ± SEM for time-resolved summary trajectories (center-of-mass displacement, mean squared displacement, and nearest-neighbor distance). Pairwise two-sided Wilcoxon rank-sum tests were used to compare ssGSEA z-scores between conditions, with Benjamini–Hochberg correction for multiple comparisons. Statistical significance was defined as $p < 0.05$.

REFERENCES

1. Miklosic, G., Ferguson, S.J., and D'Este, M. (2024). Engineering complex tissue-like microenvironments with biomaterials and biofabrication. Trends Biotechnol *42*, 1241-1257. 10.1016/j.tibtech.2024.03.008.
2. Helms, H.R., Davies, A.E., Schutt, C.E., Langer, E.M., Duhen, R., Sinawang, P.D., Akin, D., Demirci, U., Esener, S.C., Fitzgerald, R.C., and Bertassoni, L.E. (2025). Engineering and biofabrication of early cancer models. Nature Reviews Bioengineering. 10.1038/s44222-025-00371-w.
3. Bosmans, C., Gines Rodriguez, N., Gutierrez Hernandez, U.J., Fernandez Rivas, D., Karperien, M., Malda, J., Moreira Teixeira, L., Levato, R., and Leijten, J. (2025). A Quantitative Printability Framework for Programmable Assembly of Pre-Vascular Patterns via Laser-Induced Forward Transfer. Adv Healthc Mater, e03665. 10.1002/adhm.202503665.
4. Guillotin, B., Souquet, A., Catros, S., Duocastella, M., Pippenger, B., Bellance, S., Bareille, R., Remy, M., Bordenave, L., Amedee, J., and Guillemot, F. (2010). Laser assisted bioprinting of engineered tissue with high cell density and microscale organization. Biomaterials *31*, 7250-7256. 10.1016/j.biomaterials.2010.05.055.
5. Zhang, J., Byers, P., Erben, A., Frank, C., Schulte-Spechtel, L., Heymann, M., Docheva, D., Huber, H.P., Sudhop, S., and Clausen-Schaumann, H. (2021). Single Cell Bioprinting with Ultrashort Laser Pulses. Advanced Functional Materials *31*, 2100066. 10.1002/adfm.202100066.
6. Zhang, P., and Abate, A.R. (2020). High-Definition Single-Cell Printing: Cell-by-Cell Fabrication of Biological Structures. Adv Mater *32*, e2005346. 10.1002/adma.202005346.
7. Zhang, P., Liu, C., Modavi, C., Abate, A., and Chen, H. (2024). Printhead on a chip: empowering droplet-based bioprinting with microfluidics. Trends Biotechnol *42*, 353-368. 10.1016/j.tibtech.2023.09.001.
8. Kim, W., Lee, Y., Kang, D., Kwak, T., Lee, H.R., and Jung, S. (2023). 3D Inkjet-Bioprinted Lung-on-a-Chip. ACS Biomater Sci Eng *9*, 2806-2815. 10.1021/acsbiomaterials.3c00089.
9. Park, J.A., Yoon, S., Kwon, J., Now, H., Kim, Y.K., Kim, W.J., Yoo, J.Y., and Jung, S. (2017). Freeform micropatterning of living cells into cell culture medium using direct inkjet printing. Sci Rep *7*, 14610. 10.1038/s41598-017-14726-w.
10. Jeffries, G.D.M., Xu, S., Lobovkina, T., Kirejev, V., Tusseau, F., Gyllensten, C., Singh, A.K., Karila, P., Moll, L., and Orwar, O. (2020). 3D micro-organisation printing of mammalian cells to generate biological tissues. Sci Rep *10*, 19529. 10.1038/s41598-020-74191-w.
11. Gu, Y., Chen, C., Rufo, J., Shen, C., Wang, Z., Huang, P.H., Fu, H., Zhang, P., Cummer, S.A., Tian, Z., and Huang, T.J. (2020). Acoustofluidic Holography for Micro- to Nanoscale Particle Manipulation. ACS Nano *14*, 14635-14645. 10.1021/acsnano.0c03754.
12. Kirkham, G.R., Britchford, E., Upton, T., Ware, J., Gibson, G.M., Devaud, Y., Ehrbar, M., Padgett, M., Allen, S., Buttery, L.D., and Shakesheff, K. (2015). Precision assembly of complex cellular microenvironments using holographic optical tweezers. Sci Rep *5*, 8577. 10.1038/srep08577.

13. Polak, R., Zhang, E.T., and Kuo, C.J. (2024). Cancer organoids 2.0: modelling the complexity of the tumour immune microenvironment. Nat Rev Cancer *24*, 523-539. 10.1038/s41568-024-00706-6.
14. Bressan, D., Battistoni, G., and Hannon, G.J. (2023). The dawn of spatial omics. Science *381*, eabq4964. 10.1126/science.abq4964.
15. Rood, J.E., Maartens, A., Hupalowska, A., Teichmann, S.A., and Regev, A. (2022). Impact of the Human Cell Atlas on medicine. Nat Med *28*, 2486-2496. 10.1038/s41591-022-02104-7.
16. Armingol, E., Baghdassarian, H.M., and Lewis, N.E. (2024). The diversification of methods for studying cell-cell interactions and communication. Nat Rev Genet *25*, 381-400. 10.1038/s41576-023-00685-8.
17. Galon, J., Costes, A., Sanchez-Cabo, F., Kirilovsky, A., Mlecnik, B., Lagorce-Pages, C., Tosolini, M., Camus, M., Berger, A., Wind, P., et al. (2006). Type, density, and location of immune cells within human colorectal tumors predict clinical outcome. Science *313*, 1960-1964. 10.1126/science.1129139.
18. Wang, X.Q., Danenberg, E., Huang, C.S., Egle, D., Callari, M., Bermejo, B., Dugo, M., Zamagni, C., Thill, M., Anton, A., et al. (2023). Spatial predictors of immunotherapy response in triple-negative breast cancer. Nature *621*, 868-876. 10.1038/s41586-023-06498-3.
19. Garrido-Trigo, A., Corraliza, A.M., Veny, M., Dotti, I., Melon-Ardanaz, E., Rill, A., Crowell, H.L., Corbi, A., Gudino, V., Esteller, M., et al. (2023). Macrophage and neutrophil heterogeneity at single-cell spatial resolution in human inflammatory bowel disease. Nat Commun *14*, 4506. 10.1038/s41467-023-40156-6.
20. Watson, B.R., Paul, B., Rahman, R.U., Amir-Zilberstein, L., Segerstolpe, A., Epstein, E.T., Murphy, S., Geistlinger, L., Lee, T., Shih, A., et al. (2025). Spatial transcriptomics of healthy and fibrotic human liver at single-cell resolution. Nat Commun *16*, 319. 10.1038/s41467-024-55325-4.
21. Xiao, Z., Cui, L., Yuan, Y., He, N., Xie, X., Lin, S., Yang, X., Zhang, X., Shi, P., Wei, Z., et al. (2024). 3D reconstruction of a gastrulating human embryo. Cell *187*, 2855-2874 e2819. 10.1016/j.cell.2024.03.041.
22. Kim, J., Rothova, M.M., Madan, E., Rhee, S., Weng, G., Palma, A.M., Liao, L., David, E., Amit, I., Hajkarim, M.C., et al. (2023). Neighbor-specific gene expression revealed from physically interacting cells during mouse embryonic development. Proc Natl Acad Sci U S A *120*, e2205371120. 10.1073/pnas.2205371120.
23. Morse, D.B., Michalowski, A.M., Ceribelli, M., De Jonghe, J., Vias, M., Riley, D., Davies-Hill, T., Voss, T., Pittaluga, S., Muus, C., et al. (2023). Positional influence on cellular transcriptional identity revealed through spatially segmented single-cell transcriptomics. Cell Syst *14*, 464-481 e467. 10.1016/j.cels.2023.05.003.
24. Sun, E.D., Zhou, O.Y., Hauptschein, M., Rappoport, N., Xu, L., Navarro Negredo, P., Liu, L., Rando, T.A., Zou, J., and Brunet, A. (2025). Spatial transcriptomic clocks reveal cell proximity effects in brain ageing. Nature *638*, 160-171. 10.1038/s41586-024-08334-8.
25. Klughammer, J., Abravanel, D.L., Segerstolpe, A., Blosser, T.R., Goltsev, Y., Cui, Y., Goodwin, D.R., Sinha, A., Ashenberg, O., Slyper, M., et al. (2024). A multi-

modal single-cell and spatial expression map of metastatic breast cancer biopsies across clinicopathological features. Nat Med *30*, 3236-3249. 10.1038/s41591-024-03215-z.
26. Chen, W., Guillaume-Gentil, O., Rainer, P.Y., Gabelein, C.G., Saelens, W., Gardeux, V., Klaeger, A., Dainese, R., Zachara, M., Zambelli, T., et al. (2022). Live-seq enables temporal transcriptomic recording of single cells. Nature *608*, 733-740. 10.1038/s41586-022-05046-9.
27. Ainla, A., Jeffries, G.D., Brune, R., Orwar, O., and Jesorka, A. (2012). A multifunctional pipette. Lab Chip *12*, 1255-1261. 10.1039/c2lc20906c.
28. Ware, J.P. (2024). Transparency Overlay.
29. Ali, H.R., Jackson, H.W., Zanotelli, V.R.T., Danenberg, E., Fischer, J.R., Bardwell, H., Provenzano, E., Team, C.I.G.C., Rueda, O.M., Chin, S.F., et al. (2020). Imaging mass cytometry and multiplatform genomics define the phenogenomic landscape of breast cancer. Nat Cancer *1*, 163-175. 10.1038/s43018-020-0026-6.
30. Blise, K.E., Sivagnanam, S., Banik, G.L., Coussens, L.M., and Goecks, J. (2022). Single-cell spatial architectures associated with clinical outcome in head and neck squamous cell carcinoma. NPJ Precis Oncol *6*, 10. 10.1038/s41698-022-00253-z.
31. Migliozzi, S., Adabbo, B., Garofano, L., Wu, F., Davila, P., Komotar, R.J., Ivan, M.E., Shah, A.H., Currall, B.B., Williams, S., et al. (2025). Restraint of cancer cell plasticity by spatial homotypic clustering. Cancer Cell *43*, 2206-2223 e2210. 10.1016/j.ccell.2025.08.009.
32. Hanahan, D. (2022). Hallmarks of Cancer: New Dimensions. Cancer Discov *12*, 31-46. 10.1158/2159-8290.CD-21-1059.
33. Dimitrov, D., Schafer, P.S.L., Farr, E., Rodriguez-Mier, P., Lobentanzer, S., Badia, I.M.P., Dugourd, A., Tanevski, J., Ramirez Flores, R.O., and Saez-Rodriguez, J. (2024). LIANA+ provides an all-in-one framework for cell-cell communication inference. Nat Cell Biol *26*, 1613-1622. 10.1038/s41556-024-01469-w.
34. Badia, I.M.P., Velez Santiago, J., Braunger, J., Geiss, C., Dimitrov, D., Muller-Dott, S., Taus, P., Dugourd, A., Holland, C.H., Ramirez Flores, R.O., and Saez-Rodriguez, J. (2022). decoupleR: ensemble of computational methods to infer biological activities from omics data. Bioinform Adv *2*, vbac016. 10.1093/bioadv/vbac016.
35. Muller-Dott, S., Tsirvouli, E., Vazquez, M., Ramirez Flores, R.O., Badia, I.M.P., Fallegger, R., Turei, D., Laegreid, A., and Saez-Rodriguez, J. (2023). Expanding the coverage of regulons from high-confidence prior knowledge for accurate estimation of transcription factor activities. Nucleic Acids Res *51*, 10934-10949. 10.1093/nar/gkad841.
36. Schubert, M., Klinger, B., Klunemann, M., Sieber, A., Uhlitz, F., Sauer, S., Garnett, M.J., Bluthgen, N., and Saez-Rodriguez, J. (2018). Perturbation-response genes reveal signaling footprints in cancer gene expression. Nat Commun *9*, 20. 10.1038/s41467-017-02391-6.

37. Helms, H.R., and Bertassoni, L.E. (2025). Protocol for single-cell spatial transcriptomic profiling of cultured cells and engineered tissues without embedding or sectioning. STAR Protoc *6*, 104074. 10.1016/j.xpro.2025.104074.
38. Thi, K., Del Toro, K., Licon-Munoz, Y., Sayaman, R.W., and Hines, W.C. (2024). Comprehensive identification, isolation, and culture of human breast cell types. J Biol Chem *300*, 107637. 10.1016/j.jbc.2024.107637.
39. Baxter, E.W., Graham, A.E., Re, N.A., Carr, I.M., Robinson, J.I., Mackie, S.L., and Morgan, A.W. (2020). Standardized protocols for differentiation of THP-1 cells to macrophages with distinct M(IFNgamma+LPS), M(IL-4) and M(IL-10) phenotypes. J Immunol Methods *478*, 112721. 10.1016/j.jim.2019.112721.
40. Javor, J., Ewoldt, J.K., Cloonan, P.E., Chopra, A., Luu, R.J., Freychet, G., Zhernenkov, M., Ludwig, K., Seidman, J.G., Seidman, C.E., et al. (2021). Probing the subcellular nanostructure of engineered human cardiomyocytes in 3D tissue. Microsyst Nanoeng *7*, 10. 10.1038/s41378-020-00234-x.
41. Lian, X., Zhang, J., Azarin, S.M., Zhu, K., Hazeltine, L.B., Bao, X., Hsiao, C., Kamp, T.J., and Palecek, S.P. (2013). Directed cardiomyocyte differentiation from human pluripotent stem cells by modulating Wnt/beta-catenin signaling under fully defined conditions. Nat Protoc *8*, 162-175. 10.1038/nprot.2012.150.
42. Ware, J.P. (2024). Heater feedback controller.
43. Hu, Y., Becker, M.L., and Willits, R.K. (2023). Quantification of cell migration: metrics selection to model application. Front Cell Dev Biol *11*, 1155882. 10.3389/fcell.2023.1155882.
44. Wu, T., Hu, E., Xu, S., Chen, M., Guo, P., Dai, Z., Feng, T., Zhou, L., Tang, W., Zhan, L., et al. (2021). clusterProfiler 4.0: A universal enrichment tool for interpreting omics data. Innovation (Camb) *2*, 100141. 10.1016/j.xinn.2021.100141.
45. Borcherding, N., Vishwakarma, A., Voigt, A.P., Bellizzi, A., Kaplan, J., Nepple, K., Salem, A.K., Jenkins, R.W., Zakharia, Y., and Zhang, W. (2021). Mapping the immune environment in clear cell renal carcinoma by single-cell genomics. Commun Biol *4*, 122. 10.1038/s42003-020-01625-6.
46. Liberzon, A., Birger, C., Thorvaldsdottir, H., Ghandi, M., Mesirov, J.P., and Tamayo, P. (2015). The Molecular Signatures Database (MSigDB) hallmark gene set collection. Cell Syst *1*, 417-425. 10.1016/j.cels.2015.12.004.
47. Subramanian, A., Tamayo, P., Mootha, V.K., Mukherjee, S., Ebert, B.L., Gillette, M.A., Paulovich, A., Pomeroy, S.L., Golub, T.R., Lander, E.S., and Mesirov, J.P. (2005). Gene set enrichment analysis: a knowledge-based approach for interpreting genome-wide expression profiles. Proc Natl Acad Sci U S A *102*, 15545-15550. 10.1073/pnas.0506580102.
48. Dimitrov, D., Turei, D., Garrido-Rodriguez, M., Burmedi, P.L., Nagai, J.S., Boys, C., Ramirez Flores, R.O., Kim, H., Szalai, B., Costa, I.G., et al. (2022). Comparison of methods and resources for cell-cell communication inference from single-cell RNA-Seq data. Nat Commun *13*, 3224. 10.1038/s41467-022-30755-0.
49. Gu, Z., Gu, L., Eils, R., Schlesner, M., and Brors, B. (2014). circlize Implements and enhances circular visualization in R. Bioinformatics *30*, 2811-2812. 10.1093/bioinformatics/btu393.